

A Robust Hessian-based Trust Region Algorithm for Spherical Conformal Parameterizations

Zhong-Heng Tan* Tiexiang Li† Wen-Wei Lin‡ Shing-Tung Yau§

Abstract

Surface parameterizations are widely applied in computer graphics, medical imaging and transformation optics. In this paper, we rigorously derive the gradient vector and Hessian matrix of the discrete conformal energy for spherical conformal parameterizations of simply connected closed surfaces of genus-0. In addition, we give the sparsity structure of the Hessian matrix, which leads to a robust Hessian-based trust region algorithm for the computation of spherical conformal maps. Numerical experiments demonstrate the local quadratic convergence of the proposed algorithm with low conformal distortions. We subsequently propose an application of our method to surface registrations that still maintains local quadratic convergence.

Key words— spherical conformal parameterization, conformal energy minimization, Riemann surfaces of genus-0, Hessian matrix, local quadratic convergence

MSC(2020) 49Q10, 52C26, 65D18, 65F05, 68U05

1 Introduction

The Poincaré-Klein-Koebe theorem is a fundamental theorem in Riemann geometry that states that a simply connected Riemann surface \mathcal{M} is conformally equivalent to either a unit sphere \mathbb{S}^2 , a complex plane \mathbb{C} or a unit disk \mathbb{D} . From a numerical point of view, for a given discrete triangular mesh of \mathcal{M} , we require that the conformal parameterization between \mathcal{M} and the canonical shape is a bijective map from \mathcal{M} to \mathbb{S}^2 (Riemann surface of genus-zero) or \mathbb{D} (Riemann surface with a single boundary) while minimizing the total angle distortion induced by the Dirichlet energy [12, 16, 49]. Conformal parameterizations, also known as angle-preserving parameterizations, preserve the intersection angle of two arbitrary intersecting curves on the surface up to the map. In other words, conformal parameterizations preserve the local shapes of the surfaces. The development of digital 3D object technologies has enabled the representation of smooth surfaces in the real world through high-resolution meshes on computers. High-resolution meshes have the ability to characterize the intricate geometrical structure of surfaces. Nevertheless, high resolution also makes computations and processes more challenging on complicated meshes. Recently, surface parameterizations have received increasing attention due to their ability to transform intricate geometries into simply shaped regions. It is clear that the parameterization of a surface is not necessarily unique, even when the target region is given. Conformal parameterization is one of the most commonly used parameterization methods. As a result, it is used in several fields, such as medical imaging [27, 39, 31, 42], texture mapping [32, 12], and transformation optics [45, 22].

*School of Mathematics and Shing-Tung Yau Center, Southeast University, Nanjing 211189; Nanjing Center for Applied Mathematics, Nanjing 211135, People's Republic of China.

†Corresponding author. School of Mathematics and Shing-Tung Yau Center, Southeast University, Nanjing 211189; Nanjing Center for Applied Mathematics, Nanjing 211135, People's Republic of China.

‡Nanjing Center for Applied Mathematics, Nanjing 211135, People's Republic of China; Department of Applied Mathematics, Yang Ming Chiao Tung University, Hsinchu 300, Taiwan.

§Yau Mathematical Sciences Center, Tsinghua University, Beijing 100084, China.

A detailed overview of surface conformal parameterizations can be found in classical surveys [25, 9, 33, 10, 30]. Numerous methods for conformal parameterizations have been proposed, including boundary first flattening [41], discrete conformal equivalence [26], harmonic energy minimization [38] and solving the Laplacian-Beltrami equation with a particular Dirac delta function as the right-hand term [32]. In earlier years, based on the time-flow technique, Jin et al. [36] and Yang et al. [46] proposed the discrete Ricci flow with conformal circle packing metric, which is a negative gradient flow of some convex energy and can be accelerated by the Newton method. However, the evaluations of the related coefficients at each iterative step are somewhat complicated due to the circle packing metric. Huang et al. [34] proposed the quasi-implicit Euler method (QIEM) in view of the nonlinear heat diffusion process with normalization on \mathbb{S}^2 . However, the convergence can be very slow, and there is thus far no theory to support its convergence. With the great development of GPU-based computation in recent years, parallelizable algorithms were subsequently proposed [14].

In 2015, Choi et al. [15] applied the quasi-conformal approach to spherical parameterization and proposed the FLASH algorithm, which produces the composition of the quasi-conformal maps with the same Beltrami coefficient to obtain the conformal map. In 2019, Yueh et al. [48] proposed a north-south hemisphere alternating iteration, called spherical conformal energy minimization (SCEM), which alternatively maps the north and south poles to infinity and fixes the corresponding hemisphere while updating the other hemisphere. From numerical experiments, both FLASH and SCEM are satisfactory with high accuracy and effectiveness compared to those of the other previously mentioned methods. FLASH is a direct method that solves two double-sized linear systems compared to SCEM, which utilizes stereographic projection to transform the unit sphere \mathbb{S}^2 to the extended complex plane $\overline{\mathbb{C}}$. The resulting map, which is composed of the inverse stereographic projection and the computed conformal map, is the ideal conformal parameterization from the given Riemann surface of genus zero to \mathbb{S}^2 . In addition, it simplifies the spherical constraint problem in \mathbb{R}^3 into an unconstrained problem in $\overline{\mathbb{C}}$, making it highly efficient. However, the stereographic projection maps the north pole of \mathbb{S}^2 to infinity and others to \mathbb{C} . Therefore, the computational error near the north pole becomes relatively large in practical applications. To mitigate this error, the north-south hemisphere alternatingly iterative SCEM reduces the conformal distortion near the poles and has numerically sublinear convergence and asymptotically R -linear convergence. However, larger computational errors in conformal quantities are transferred to the junction of the equator. From a theoretical point of view, both FLASH and SCEM consider minimizing the Dirichlet energy on the extended complex plane $\overline{\mathbb{C}}$. From a numerical point of view, both FLASH and SCEM may get larger angle distortions near the junction region of the computational conformal map because they are connected by two submaps via stereographic projection.

Different from FLASH and SCEM, in this paper, we solve the spherical conformal energy optimization problem to obtain the conformal map by directly employing the spherical coordinates for the representation of the conformal energy. Unlike the stereographic projection, the spherical coordinate representation is not a conformal map. We derive the related gradient vector and Hessian matrix and develop a robust Hessian-based trust region (HBTR) algorithm that has local quadratic convergence. The main contributions of this paper can be divided into three folds.

- We use the spherical coordinates to represent the conformal energy on \mathbb{S}^2 and develop the HBTR algorithm to directly minimize the discrete conformal energy, which is described as the difference between the discrete Dirichlet energy on \mathbb{S}^2 and the image area of the conformal map. In Section 5.3, numerical experiments demonstrate that the discrete conformal energy, mean and standard deviation (SD) are reduced to 1/4 and 1/2, respectively, when the mesh size is refined by a half.
- We give the explicit derivation of the gradient vector and Hessian matrix and present the significant sparsity of the Hessian matrix. This benefits the development of fast computations for calculating the Newton iterations. Combined with the trust region technique, we thus propose the robust HBTR algorithm.

- Numerical experiments and comparisons with existing algorithms demonstrate the advantages of our method in terms of conformality and robustness. The computational cost of the HBTR algorithm is of the same order of magnitude as that of FLASH and SCEM but slightly more expensive for most models due to spending a high percentage of time selecting the convergence region. Furthermore, the bijectivity can almost be guaranteed because the conformal energy is expressed by the unity of spherical coordinates. For few meshes resulting in nonbijective maps, folding can be easily removed by performing a postprocessing algorithm [24].

This paper is organized as follows. The Section 2 provides a brief review of the conformal map and conformal energy. Then, in Section 3 we present the theoretical derivation of the gradient vector and Hessian matrix. In Section 4, we describe the proposed algorithm for spherical conformal parameterization that uses the sparsity property of the Hessian matrix. The numerical performance and comparison with other methods are presented in Section 5. In Section 6, we demonstrate an application of the algorithm to surface registration. A concluding mark is given in Section 7.

The frequently used notations in this paper are listed here. Bold letters, e.g., \mathbf{a}, \mathbf{s} denote vectors. \mathbf{a}_i denotes the i -th entry of \mathbf{a} . $\mathbf{1}_{m \times n}$ denotes the $m \times n$ matrix of all ones. The notation without subscript $\mathbf{1}$ denotes the vector of all ones with proper dimension. \mathbf{e}_i denotes the i -th column of the identity matrix with the proper dimension. $[A]_{ij}$ denotes the (i, j) -th entry of matrix A . $\text{diag}(\mathbf{a})$ denotes the diagonal matrix with the (i, i) -th entry being \mathbf{a}_i . $[v_i, v_j]$ denotes the edge formed by v_i and v_j . $[v_i, v_j, v_k]$ denotes the triangle formed by v_i, v_j and v_k , and $|[v_i, v_j, v_k]|$ denotes the area of that triangle. The other notations are defined wherever they appear.

2 Conformal map and Conformal Energy

In this section, we briefly review the continuous conformal map and the conformal energy. Readers can refer to [28, 29, 35, 40, 32] for more details.

Let $\mathcal{M} = \mathbf{r}(u, v)$ be a surface and f be a continuous and bijective vector-valued map on \mathcal{M} , which maps \mathcal{M} to another surface $\widetilde{\mathcal{M}} = \widetilde{\mathbf{r}}(u, v)$ with $(u, v) \in \Omega \subset \mathbb{R}^2$. Let $\gamma_1, \gamma_2 \subset \mathcal{M}$ be two arbitrary curves intersecting at a point. Then, we call f conformal if the intersecting angle of γ_1 and γ_2 equals that of $f(\gamma_1)$ and $f(\gamma_2)$ in $\widetilde{\mathcal{M}}$. Equivalently, f is conformal if and only if the first fundamental forms $I(u, v)$ and $\widetilde{I}(u, v)$ of \mathcal{M} and $\widetilde{\mathcal{M}}$ with respect to (u, v) , i.e.,

$$I(u, v) = \begin{bmatrix} \langle \mathbf{r}_u, \mathbf{r}_u \rangle & \langle \mathbf{r}_u, \mathbf{r}_v \rangle \\ \langle \mathbf{r}_v, \mathbf{r}_u \rangle & \langle \mathbf{r}_v, \mathbf{r}_v \rangle \end{bmatrix}, \quad \widetilde{I}(u, v) = \begin{bmatrix} \langle \widetilde{\mathbf{r}}_u, \widetilde{\mathbf{r}}_u \rangle & \langle \widetilde{\mathbf{r}}_u, \widetilde{\mathbf{r}}_v \rangle \\ \langle \widetilde{\mathbf{r}}_v, \widetilde{\mathbf{r}}_u \rangle & \langle \widetilde{\mathbf{r}}_v, \widetilde{\mathbf{r}}_v \rangle \end{bmatrix},$$

satisfy

$$\widetilde{I}(u, v) = \eta(u, v)I(u, v),$$

where $\mathbf{r}_u := \frac{\partial \mathbf{r}}{\partial u}$, $\mathbf{r}_v := \frac{\partial \mathbf{r}}{\partial v}$ and $\eta(u, v)$ is a positive scalar function on Ω . Then, the conformal energy functional [35] of f is defined as

$$E_C(f) = \frac{1}{2} \int_{\mathcal{M}} \|\nabla_{\mathcal{M}} f\|_F^2 d\sigma - \mathcal{A}(f), \quad (2.1)$$

where $\nabla_{\mathcal{M}}$ is the tangential gradient, $d\sigma$ is the area element on \mathcal{M} and $\mathcal{A}(f)$ is the area of the image surface $\widetilde{\mathcal{M}} = f(\mathcal{M})$. Let us note that the first term in (2.1) is the Dirichlet energy functional of f . It has been proven that [35, 40]

- $E_C(f) \geq 0$,
- $E_C(f) = 0$ if and only if f is conformal.

From these properties, it is reasonable to adopt conformal energy minimization (CEM) to obtain the conformal map. In the continuous scheme, if the target surface $\widetilde{\mathcal{M}}$ is given, its area remains constant. Thus, a method to solve (2.1) is to minimize the Dirichlet energy, which is a quadratic functional. In the discrete scheme, the area is actually not a constant. Introducing the discrete area term typically yields a better conformal parameterization. It is easy to verify that the optimization

problem (2.1) has a trivial solution $f = \text{constant}$. In this case, all vertices shrink into a point, and the area of the formed region becomes 0, which violates the requirement of f being bijective. We refer to the trivial solution as 'degeneration'. Directly minimizing the Dirichlet energy without any additional constraints often leads to degeneration in practical computations. The area term is a natural penalty for the parameterization and hence can greatly weaken the degeneration during iteration [35]. On the other hand, introducing the area term can further decrease the conformal distortion. For disk parameterizations, Yueh et al.[49] proposed a disk conformal parameterization algorithm through Dirichlet energy minimization, while a novel algorithm minimizing the disk conformal energy was later proposed by Kuo et al. [37], in which they derived a particular and simple area expression of a discrete disk represented by polar coordinates to design a fast algorithm. As a consequence, conformal energy minimization [37] gives significantly less conformal energy and angle distortion compared to those of the Dirichlet energy minimization [49].

For the spherical parameterization, it is clearly feasible to introduce the area term. However, it is a significant challenge that the area of the discrete sphere, which is the sum of areas of all triangles formed by vertices, cannot be simply expressed as in the disk case, even if both vertices are of unit length. Simultaneously, the gradient vector and Hessian matrix of the conformal energy also have complicated expressions. In the next section, we carefully derive the expression of the conformal energy for the spherical parameterization with spherical coordinates, along with its gradient vector and Hessian matrix. The Hessian matrix has a special sparsity structure as the Laplacian matrix, which guides the fast construction and computation associated with it.

3 Discrete Conformal Energy on Closed Surfaces

Let M be a discrete closed surface of genus-0 composed of triangles, called a triangulation. Given that M has n vertices, we denote the vertex set, edge set and triangle face set of M by $\mathcal{V}(M) = \{v_i, i = 1, 2, \dots, n\}$, $\mathcal{E}(M) = \{[v_i, v_j]\}$ and $\mathcal{F}(M) = \{T_{ijk} := [v_i, v_j, v_k]\}$, respectively.

In this paper, we aim to find a piecewise linear map f that maps surface M to a discrete unit sphere \mathbb{S}^2 conformally, in which all of the vertices are unit vectors. Every point in a triangle can be represented as the convex combination of its vertices via barycentric coordinates,

$$f(\hat{v}) = \lambda_i(\hat{v})f(v_i) + \lambda_j(\hat{v})f(v_j) + \lambda_k(\hat{v})f(v_k), \text{ for } \hat{v} \in T_{ijk}, \quad (3.1)$$

where

$$\lambda_i(\hat{v}) = \frac{|[\hat{v}, v_j, v_k]|}{|T_{ijk}|}, \quad \lambda_j(\hat{v}) = \frac{|[v_i, \hat{v}, v_k]|}{|T_{ijk}|}, \quad \lambda_k(\hat{v}) = \frac{|[v_i, v_j, \hat{v}]|}{|T_{ijk}|}.$$

After $f(v_i), i = 1, 2, \dots, n$ is obtained, the discrete sphere is also formed. Hence, we compute $\mathbf{f} = [\mathbf{f}_1^\top, \mathbf{f}_2^\top, \dots, \mathbf{f}_n^\top]^\top \in \mathbb{R}^{n \times 3}$ with $\mathbf{f}_i = f(v_i) \in \mathbb{R}^{1 \times 3}$ for the given triangulation of M .

From the perspective of the conformal energy (2.1), the conformal map f is obtained by solving the optimization problem

$$\mathbf{f}^* = \underset{\mathbf{f}: \|\mathbf{f}_i\|=1, i=1,2,\dots,n}{\operatorname{argmin}} E_C(f), \quad (3.2)$$

where the discrete conformal energy $E_C(f)$ of f on M is given by

$$E_C(f) = \frac{1}{2} \langle L\mathbf{f}, \mathbf{f} \rangle - A(f), \quad (3.3)$$

in which L is the Laplacian matrix defined as

$$[L]_{ij} = \begin{cases} -w_{ij} & \text{if } i \neq j, [v_i, v_j] \in \mathcal{E}(M), \\ \sum_{k \in \mathcal{N}(i)} w_{ik} & \text{if } i = j, \\ 0 & \text{if } [v_i, v_j] \notin \mathcal{E}(M), \end{cases} \quad (3.4)$$

with cotangent weights $w_{ij} = \frac{1}{2}(\cot \alpha_{ij} + \cot \alpha_{ji})$. Here, α_{ij} and α_{ji} are the angles opposite to the edge $[v_i, v_j]$ ¹ and $\mathcal{N}(i)$ is the index set of the adjacent vertices v_i , as shown in fig. 1. Readers can

¹A closed surface has no boundary. Therefore, an edge must correspond to 2 opposite angles.

refer to [29, Chap. 24] for a detailed derivation of the discrete Dirichlet energy on triangulation. $A(f)$ in (3.3) is the area of the triangulation $f(M)$, which can be written as the sum of areas of all triangles in $f(M)$, that is, $A(f) = \sum_{T_{ijk} \in \mathcal{F}(M)} |f(T_{ijk})|$.

Let $v_{ij} = v_i - v_j$ and $\mathbf{f}_{ij} = \mathbf{f}_i - \mathbf{f}_j$ for simplicity, $\alpha_{ij}(f)$ and $\alpha_{ki}(f)$ be the angle, respectively, opposite to the edges $[\mathbf{f}_i, \mathbf{f}_j]$ and $[\mathbf{f}_k, \mathbf{f}_i] \in \mathcal{E}(f(M))$. And let $L(f)$ be a Laplacian matrix with respect to f as L , by replacing the cotangent weights as $w_{ij}(f) = \frac{1}{2}(\cot \alpha_{ij}(f) + \cot \alpha_{ji}(f))$ in the target sphere \mathbb{S}^2 . $A(f)$ and its gradient with respect to \mathbf{f} can be represented as in the following lemma.

Lemma 1. *The area of the image of f and its gradient can be represented as*

$$\begin{aligned} A(f) &= \frac{1}{2} \langle L(f) \mathbf{f}, \mathbf{f} \rangle, \\ \nabla_{\mathbf{f}} A(f) &= L(f) \mathbf{f}. \end{aligned}$$

Proof. The area of a triangle $f(T_{ijk}) \in \mathcal{F}(f(M))$ can be calculated by

$$\begin{aligned} |f(T_{ijk})| &= \frac{1}{2} \|\mathbf{f}_{ij} \times \mathbf{f}_{jk}\| = \frac{\|\mathbf{f}_{ij} \times \mathbf{f}_{jk}\|^2}{4|f(T_{ijk})|} \\ &= \frac{\langle \mathbf{f}_{jk} \times (\mathbf{f}_{ij} \times \mathbf{f}_{jk}), \mathbf{f}_{ij} \rangle}{4|f(T_{ijk})|} = \frac{\langle \mathbf{f}_{jk} \times (\mathbf{f}_{ki} \times \mathbf{f}_{ij}), \mathbf{f}_{ij} \rangle}{4|f(T_{ijk})|} \end{aligned} \quad (3.5)$$

$$= \frac{\langle \langle \mathbf{f}_{ij}, \mathbf{f}_{jk} \rangle \mathbf{f}_{ki} - \langle \mathbf{f}_{jk}, \mathbf{f}_{ki} \rangle \mathbf{f}_{ij}, \mathbf{f}_{ij} \rangle}{4|f(T_{ijk})|} \quad (3.6)$$

$$\begin{aligned} &= -\frac{\langle \mathbf{f}_{ki}, \mathbf{f}_{ij} \rangle \langle \mathbf{f}_{jk}, \mathbf{f}_{jk} \rangle + \langle \mathbf{f}_{ij}, \mathbf{f}_{jk} \rangle \langle \mathbf{f}_{ki}, \mathbf{f}_{ki} \rangle + \langle \mathbf{f}_{jk}, \mathbf{f}_{ki} \rangle \langle \mathbf{f}_{ij}, \mathbf{f}_{ij} \rangle}{8|f(T_{ijk})|} \\ &= \frac{1}{4} (\cot \alpha_{jk}(f) \|\mathbf{f}_{jk}\|^2 + \cot \alpha_{ki}(f) \|\mathbf{f}_{ki}\|^2 + \cot \alpha_{ij}(f) \|\mathbf{f}_{ij}\|^2), \end{aligned} \quad (3.7)$$

In the last equation (3.7), we use the formula $\cot \alpha_{ij}(f) = -\frac{\langle \mathbf{f}_{jk}, \mathbf{f}_{ki} \rangle}{2|T_{ijk}|}$. Hence, the area $A(f)$ can be represented as

$$\begin{aligned} A(f) &= \sum_{T_{ijk} \in \mathcal{F}(M)} |f(T_{ijk})| \\ &= \frac{1}{4} \sum_{T_{ijk} \in \mathcal{F}(M)} (\cot \alpha_{jk}(f) \|\mathbf{f}_{jk}\|^2 + \cot \alpha_{ki}(f) \|\mathbf{f}_{ki}\|^2 + \cot \alpha_{ij}(f) \|\mathbf{f}_{ij}\|^2) \\ &= \frac{1}{2} \sum_{ij: [v_i, v_j] \in \mathcal{E}(M)} w_{ij}(f) \|\mathbf{f}_{ij}\|^2 = \frac{1}{2} \langle L(f) \mathbf{f}, \mathbf{f} \rangle. \end{aligned}$$

Then, by using the derivation of (3.5)-(3.6), we have

$$\begin{aligned} \frac{\partial |f(T_{ijk})|}{\partial \mathbf{f}_i} &= \frac{2\mathbf{f}_{jk} \times (\mathbf{f}_{ij} \times \mathbf{f}_{jk})}{8|f(T_{ijk})|} = \frac{\langle \mathbf{f}_{ij}, \mathbf{f}_{jk} \rangle \mathbf{f}_{ki} - \langle \mathbf{f}_{jk}, \mathbf{f}_{ki} \rangle \mathbf{f}_{ij}}{4|f(T_{ijk})|} \\ &= \frac{1}{2} (\cot \alpha_{ij}(f) \mathbf{f}_{ij} - \cot \alpha_{ki}(f) \mathbf{f}_{ki}) \in \mathbb{R}^{1 \times 3}, \end{aligned} \quad (3.8)$$

Hence, the derivative of $A(f)$ with respect to \mathbf{f}_i is

$$\frac{\partial A(f)}{\partial \mathbf{f}_i} = \sum_{T_{ijk} \in \mathcal{F}(M)} \frac{\partial |f(T_{ijk})|}{\partial \mathbf{f}_i} = \frac{1}{2} \sum_{T_{ijk} \in \mathcal{F}(M)} (\cot \alpha_{ij}(f) \mathbf{f}_{ij} - \cot \alpha_{ki}(f) \mathbf{f}_{ki}) = \mathbf{e}_i^\top L(f) \mathbf{f},$$

for $i = 1, 2, \dots, n$. This completes the proof. \square

From (3.3) and Lemma 1, we have

$$E_C(f) = \frac{1}{2} \langle D(f) \mathbf{f}, \mathbf{f} \rangle, \quad \text{with } D(f) = L - L(f), \quad (3.9)$$

$$\nabla_{\mathbf{f}} E_C(f) = D(f) \mathbf{f}. \quad (3.10)$$

Clearly, $D(f)$ has the same sparsity structure as L and $L(f)$, and the corresponding cotangent weight is $[D(f)]_{ij} := \tilde{w}_{ij} = w_{ij} - w_{ij}(f)$.

Remark 1. *If f^* is a conformal map, the inner angles of the triangles in M are identical to those in $f^*(M)$. We have $w_{ij}(f^*) = w_{ij}$ and $D(f) = \mathbf{0}$, which leads to $E_C(f^*) = 0$.*

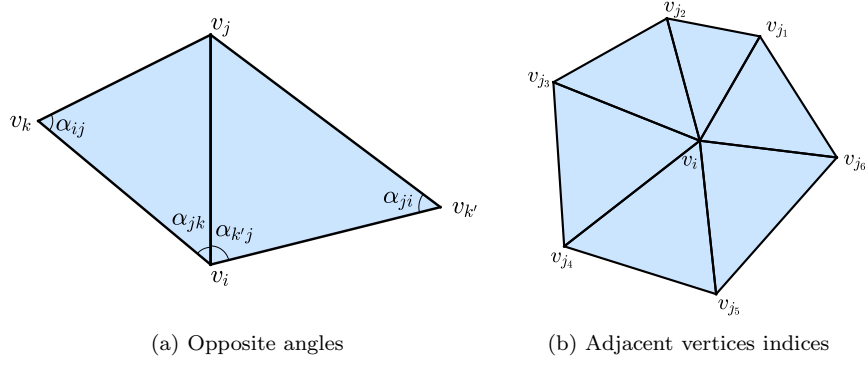


Figure 1: Illustrations of opposite angles and adjacent vertices indices set. (a) α_{ij} and α_{ji} are the pair of opposite angles of edge $[v_i, v_j]$; α_{jk} and $\alpha_{k'j}$ are the opposite angles of edge $[v_j, v_k]$ in T_{ijk} and $[v_{k'}, v_j]$ in $T_{k'ji}$, respectively. (b) v_{j_1}, \dots, v_{j_6} are the adjacent vertices of v_i . Hence, $\mathcal{N}(i) = \{j_1, j_2, \dots, j_6\}$.

Let $\mathbf{f} = [\mathbf{x}, \mathbf{y}, \mathbf{z}]$ and $\text{vec}(\mathbf{f}) = [\mathbf{x}^\top, \mathbf{y}^\top, \mathbf{z}^\top]^\top$ be its vectorization. Since the vertices of \mathbf{f} are on the sphere, we adopt the spherical coordinates to represent all vertices by

$$\mathbf{x} = \cos \boldsymbol{\theta} \odot \sin \boldsymbol{\phi}, \quad \mathbf{y} = \sin \boldsymbol{\theta} \odot \sin \boldsymbol{\phi}, \quad \mathbf{z} = \cos \boldsymbol{\phi}, \quad (3.11a)$$

and let

$$\mathbf{u} = \cos \boldsymbol{\theta} \odot \cos \boldsymbol{\phi}, \quad \mathbf{v} = \sin \boldsymbol{\theta} \odot \cos \boldsymbol{\phi}, \quad \mathbf{w} = \sin \boldsymbol{\phi}, \quad (3.11b)$$

where $\boldsymbol{\theta}, \boldsymbol{\phi} \in \mathbb{R}^n$ are the azimuth and elevation angle vectors of the corresponding vertices of \mathbf{f} , respectively, and \odot is the Hadamard product. Similar to the stereographic projection in [48, 15], the spherical coordinate representation eliminates the unit-length constraint and transforms the Cartesian coordinate $[\mathbf{x}, \mathbf{y}, \mathbf{z}]$ into the spherical coordinate $[\boldsymbol{\theta}, \boldsymbol{\phi}]$, reducing the input variable scale by 1/3. Furthermore, the spherical coordinate projects the whole sphere into a bounded region $[0, 2\pi] \times [0, \pi]$, which avoids the computational error near the north pole [15] or the equator [48] by using the stereographic projection. In the further discussion, we denote that $\nabla := [\nabla_{\boldsymbol{\theta}}^\top, \nabla_{\boldsymbol{\phi}}^\top]^\top$ with respect to $(\boldsymbol{\theta}, \boldsymbol{\phi})$ unless a special illustration in the rest of the paper. The gradient of any scalar a and Jacobi matrix of any vector \mathbf{a} with respect to $(\boldsymbol{\theta}, \boldsymbol{\phi})$ are represented as

$$\nabla a = \left[\frac{\partial a}{\partial \theta_1}, \dots, \frac{\partial a}{\partial \theta_n}, \frac{\partial a}{\partial \phi_1}, \dots, \frac{\partial a}{\partial \phi_n} \right]^\top, \quad \nabla \mathbf{a} = \left[\frac{\partial \mathbf{a}}{\partial \theta_1}, \dots, \frac{\partial \mathbf{a}}{\partial \theta_n}, \frac{\partial \mathbf{a}}{\partial \phi_1}, \dots, \frac{\partial \mathbf{a}}{\partial \phi_n} \right],$$

respectively. Furthermore, the gradient of $\mathbf{x}, \mathbf{y}, \mathbf{z}, \mathbf{u}, \mathbf{v}, \mathbf{w}$ can be represented by themselves,

$$\begin{aligned} \nabla \mathbf{x} &= [-\text{diag}(\mathbf{y}), \text{diag}(\mathbf{u})], & \nabla \mathbf{y} &= [\text{diag}(\mathbf{x}), \text{diag}(\mathbf{v})], & \nabla \mathbf{z} &= [\mathbf{0}_{n \times n}, -\text{diag}(\mathbf{w})], \\ \nabla \mathbf{u} &= [-\text{diag}(\mathbf{v}), -\text{diag}(\mathbf{x})], & \nabla \mathbf{v} &= [\text{diag}(\mathbf{u}), -\text{diag}(\mathbf{y})], & \nabla \mathbf{w} &= [\mathbf{0}_{n \times n}, \text{diag}(\mathbf{z})]. \end{aligned} \quad (3.12)$$

We now vectorize the gradient (3.10) and let

$$\mathbf{p} = D(f)\mathbf{x}, \quad \mathbf{q} = D(f)\mathbf{y}, \quad \mathbf{r} = D(f)\mathbf{z}. \quad (3.13)$$

From (3.9), we have $E_C(f) = \frac{1}{2}(\mathbf{x}^\top \mathbf{p} + \mathbf{y}^\top \mathbf{q} + \mathbf{z}^\top \mathbf{r})$. Then, from (3.10) and (3.12), the gradient of $E_C(f)$ with respect to $(\boldsymbol{\theta}, \boldsymbol{\phi})$ is

$$\mathbf{g} := \nabla E_C = \nabla \text{vec}(\mathbf{f})^\top \nabla_{\text{vec}(\mathbf{f})} E_C \quad (3.14)$$

$$= \nabla \mathbf{x}^\top \mathbf{p} + \nabla \mathbf{y}^\top \mathbf{q} + \nabla \mathbf{z}^\top \mathbf{r} = \begin{bmatrix} -\text{diag}(\mathbf{y})\mathbf{p} + \text{diag}(\mathbf{x})\mathbf{q} \\ \text{diag}(\mathbf{u})\mathbf{p} + \text{diag}(\mathbf{v})\mathbf{q} - \text{diag}(\mathbf{w})\mathbf{r} \end{bmatrix} \in \mathbb{R}^{2n \times 1}. \quad (3.15)$$

Moreover, the Hessian matrix is also obtained

$$\begin{aligned} H := \nabla \nabla E_C &= (\nabla \mathbf{x}^\top \nabla \mathbf{p} + \nabla \mathbf{y}^\top \nabla \mathbf{q} + \nabla \mathbf{z}^\top \nabla \mathbf{r}) \\ &+ \begin{bmatrix} -\text{diag}(\mathbf{p})\nabla \mathbf{y} + \text{diag}(\mathbf{q})\nabla \mathbf{x} \\ \text{diag}(\mathbf{p})\nabla \mathbf{u} + \text{diag}(\mathbf{q})\nabla \mathbf{v} - \text{diag}(\mathbf{r})\nabla \mathbf{w} \end{bmatrix} \in \mathbb{R}^{2n \times 2n}, \end{aligned} \quad (3.16)$$

where

$$\nabla \mathbf{p} = D(f)\nabla \mathbf{x} - \sum_{\ell=1}^n \mathbf{x}_\ell \nabla(L(f)\mathbf{e}_\ell), \quad \nabla \mathbf{q} = D(f)\nabla \mathbf{y} - \sum_{\ell=1}^n \mathbf{y}_\ell \nabla(L(f)\mathbf{e}_\ell), \quad \nabla \mathbf{r} = D(f)\nabla \mathbf{z} - \sum_{\ell=1}^n \mathbf{z}_\ell \nabla(L(f)\mathbf{e}_\ell).$$

Via the chain rule

$$\nabla(L(f)\mathbf{e}_\ell) = \nabla_{\mathbf{x}}(L(f)\mathbf{e}_\ell)\nabla \mathbf{x} + \nabla_{\mathbf{y}}(L(f)\mathbf{e}_\ell)\nabla \mathbf{y} + \nabla_{\mathbf{z}}(L(f)\mathbf{e}_\ell)\nabla \mathbf{z} \in \mathbb{R}^{n \times 2n},$$

we have

$$\begin{bmatrix} \sum_{\ell=1}^n \mathbf{x}_\ell \nabla(L(f)\mathbf{e}_\ell) \\ \sum_{\ell=1}^n \mathbf{y}_\ell \nabla(L(f)\mathbf{e}_\ell) \\ \sum_{\ell=1}^n \mathbf{z}_\ell \nabla(L(f)\mathbf{e}_\ell) \end{bmatrix} = \begin{bmatrix} \sum_{\ell=1}^n \mathbf{x}_\ell \nabla_{\mathbf{x}}(L(f)\mathbf{e}_\ell) & \sum_{\ell=1}^n \mathbf{x}_\ell \nabla_{\mathbf{y}}(L(f)\mathbf{e}_\ell) & \sum_{\ell=1}^n \mathbf{x}_\ell \nabla_{\mathbf{z}}(L(f)\mathbf{e}_\ell) \\ \sum_{\ell=1}^n \mathbf{y}_\ell \nabla_{\mathbf{x}}(L(f)\mathbf{e}_\ell) & \sum_{\ell=1}^n \mathbf{y}_\ell \nabla_{\mathbf{y}}(L(f)\mathbf{e}_\ell) & \sum_{\ell=1}^n \mathbf{y}_\ell \nabla_{\mathbf{z}}(L(f)\mathbf{e}_\ell) \\ \sum_{\ell=1}^n \mathbf{z}_\ell \nabla_{\mathbf{x}}(L(f)\mathbf{e}_\ell) & \sum_{\ell=1}^n \mathbf{z}_\ell \nabla_{\mathbf{y}}(L(f)\mathbf{e}_\ell) & \sum_{\ell=1}^n \mathbf{z}_\ell \nabla_{\mathbf{z}}(L(f)\mathbf{e}_\ell) \end{bmatrix} \begin{bmatrix} \nabla \mathbf{x} \\ \nabla \mathbf{y} \\ \nabla \mathbf{z} \end{bmatrix}. \quad (3.17)$$

Plugging (3.17) into (3.16), we can rewrite the Hessian matrix as

$$H = \begin{bmatrix} \nabla \mathbf{x} \\ \nabla \mathbf{y} \\ \nabla \mathbf{z} \end{bmatrix}^\top (L_1 - L_2) \begin{bmatrix} \nabla \mathbf{x} \\ \nabla \mathbf{y} \\ \nabla \mathbf{z} \end{bmatrix} - \begin{bmatrix} \text{diag}(\mathbf{p} \odot \mathbf{x} + \mathbf{q} \odot \mathbf{y}) & \text{diag}(\mathbf{p} \odot \mathbf{v} - \mathbf{q} \odot \mathbf{u}) \\ \text{diag}(\mathbf{p} \odot \mathbf{v} - \mathbf{q} \odot \mathbf{u}) & \text{diag}(\mathbf{p} \odot \mathbf{x} + \mathbf{q} \odot \mathbf{y} + \mathbf{r} \odot \mathbf{z}) \end{bmatrix} \quad (3.18)$$

$$\equiv H_1 - H_2 - K, \quad (3.19)$$

where

$$H_s = \begin{bmatrix} \nabla \mathbf{x}^\top & \nabla \mathbf{y}^\top & \nabla \mathbf{z}^\top \end{bmatrix} L_s \begin{bmatrix} \nabla \mathbf{x} \\ \nabla \mathbf{y} \\ \nabla \mathbf{z} \end{bmatrix}, \quad s = 1, 2,$$

$$K = \begin{bmatrix} \text{diag}(\mathbf{p} \odot \mathbf{x} + \mathbf{q} \odot \mathbf{y}) & \text{diag}(\mathbf{p} \odot \mathbf{v} - \mathbf{q} \odot \mathbf{u}) \\ \text{diag}(\mathbf{p} \odot \mathbf{v} - \mathbf{q} \odot \mathbf{u}) & \text{diag}(\mathbf{p} \odot \mathbf{x} + \mathbf{q} \odot \mathbf{y} + \mathbf{r} \odot \mathbf{z}) \end{bmatrix}$$

with

$$L_1 = \begin{bmatrix} D(f) & & \\ & D(f) & \\ & & D(f) \end{bmatrix}, \quad L_2 = \begin{bmatrix} \sum_{\ell=1}^n \mathbf{x}_\ell \nabla_{\mathbf{x}}(L(f)\mathbf{e}_\ell) & \sum_{\ell=1}^n \mathbf{x}_\ell \nabla_{\mathbf{y}}(L(f)\mathbf{e}_\ell) & \sum_{\ell=1}^n \mathbf{x}_\ell \nabla_{\mathbf{z}}(L(f)\mathbf{e}_\ell) \\ \sum_{\ell=1}^n \mathbf{y}_\ell \nabla_{\mathbf{x}}(L(f)\mathbf{e}_\ell) & \sum_{\ell=1}^n \mathbf{y}_\ell \nabla_{\mathbf{y}}(L(f)\mathbf{e}_\ell) & \sum_{\ell=1}^n \mathbf{y}_\ell \nabla_{\mathbf{z}}(L(f)\mathbf{e}_\ell) \\ \sum_{\ell=1}^n \mathbf{z}_\ell \nabla_{\mathbf{x}}(L(f)\mathbf{e}_\ell) & \sum_{\ell=1}^n \mathbf{z}_\ell \nabla_{\mathbf{y}}(L(f)\mathbf{e}_\ell) & \sum_{\ell=1}^n \mathbf{z}_\ell \nabla_{\mathbf{z}}(L(f)\mathbf{e}_\ell) \end{bmatrix}. \quad (3.20)$$

In the matrix L_2 , the Jacobian matrix of each column of $L(f)$ should be considered. For the ℓ -th column entries $L(f)\mathbf{e}_\ell$, it is clear that $[L(f)]_{i\ell} \neq 0$ if and only if $i \in \mathcal{N}(\ell)$ or $i = \ell$ by the definition of the Laplacian matrix in (3.4). The nondiagonal entries are negative cotangent weights, and the diagonal entries are the sums of the cotangent weights. Hence, the Jacobian matrix of $L(f)\mathbf{e}_\ell$ is formed by the gradient of cotangent weights $w_{ij}(f)$, especially the gradient of cotangent functions $c_{ij}(f) := \cot \alpha_{ij}(f)$. Before discussing entries of $\nabla L\mathbf{e}_\ell$, we first give a lemma for the sparsity structure of the Jacobian block $\sum_{\ell=1}^n \mathbf{a}_\ell \nabla_{\mathbf{b}}(L(f)\mathbf{e}_\ell)$, $\mathbf{a}, \mathbf{b} = \mathbf{x}, \mathbf{y}, \mathbf{z}$.

Lemma 2. *Each subblock $\sum_{\ell=1}^n \mathbf{a}_\ell \nabla_{\mathbf{b}}(L(f)\mathbf{e}_\ell)$ of L_2 in (3.20) with $\mathbf{a}, \mathbf{b} = \mathbf{x}, \mathbf{y}, \mathbf{z}$ is of identical sparsity structure to L .*

Proof. By the cotangent formula in (3.8), one can observe that the gradients with respect to $\mathbf{x}, \mathbf{y}, \mathbf{z}$ are the 1st, 2nd and 3rd entries of that with respect to \mathbf{f} , respectively. Hence, $\sum_{\ell=1}^n \mathbf{a}_\ell \nabla_{\mathbf{b}}(L(f)\mathbf{e}_\ell)$ has identical sparsity for all $\mathbf{a}, \mathbf{b} = \mathbf{x}, \mathbf{y}, \mathbf{z}$. Here, we denote the nonzero indices set of $\mathbf{e}_i^\top \nabla_{\mathbf{b}}(L(f)\mathbf{e}_j)$ as

$$S(i, j) = \{k \mid [\nabla_{\mathbf{b}}(L(f)\mathbf{e}_j)]_{ik} \neq 0\}.$$

Clearly, the nonzero indices set of $\mathbf{e}_i^\top \sum_{\ell=1}^n \mathbf{a}_\ell \nabla_{\mathbf{b}}(L(f)\mathbf{e}_\ell)$ is $\bigcup_{\ell=1}^n S(i, \ell)$.

- For $i \neq j$ and $[v_i, v_j] \notin \mathcal{E}(M)$, the entries are 0, and therefore, the gradients are also 0. Hence,

$$S(i, j) = \emptyset. \quad (3.21)$$

- For $i \neq j$ and $[v_i, v_j] \in \mathcal{E}(M)$, by the definition of cotangent weight $w_{ij}(f) = \frac{1}{2}(c_{ij}(f) + c_{ji}(f))$, we have $\mathbf{e}_i^\top \nabla_{\mathbf{b}}(L(f)\mathbf{e}_j) = -\nabla_{\mathbf{b}}w_{ij}(f) = -\frac{1}{2}(\nabla_{\mathbf{b}}c_{ij}(f) + \nabla_{\mathbf{b}}c_{ji}(f))$. As shown in Figure 1a, one can see that $w_{ij}(f)$ relates to only 4 vertices $\mathbf{f}_i, \mathbf{f}_j, \mathbf{f}_k, \mathbf{f}_{k'}$. Therefore, the entries of $\nabla_{\mathbf{b}}w_{ij}(f)$ are 0 except for the i, j, k, k' -th entries; that is,

$$S(i, j) = \{i, j, k, k'\} \subset \mathcal{N}(i) \cup \{i\}. \quad (3.22)$$

- For $i = j$, we have $\mathbf{e}_i^\top \nabla_{\mathbf{b}}(L(f)\mathbf{e}_i) = \nabla_{\mathbf{b}}[L(f)]_{ii} = \sum_{j \in \mathcal{N}(i)} \nabla_{\mathbf{b}}w_{ij}(f)$. Hence, we can easily verify that $\mathbf{e}_i^\top \nabla_{\mathbf{b}}(L_f\mathbf{e}_i)$ relates to the whole adjacent vertices of \mathbf{f}_i from Figure 1b. It immediately follows that

$$S(i, i) = \mathcal{N}(i) \cup \{i\}. \quad (3.23)$$

Combining (3.21), (3.22) and (3.23), we have $S(i, \ell) \subset \mathcal{N}(i) \cup \{i\} = S(i, i)$, for $\ell \neq i$. It follows that $\bigcup_{\ell=1}^n S(i, \ell) = S(i, i) = \mathcal{N}(i) \cup \{i\}$. Since the index set of nonzero entries of $\mathbf{e}_i^\top L$ is $\mathcal{N}(i) \cup \{i\}$, the lemma is obtained immediately. \square

The Lemma 2 demonstrates that $[\sum_{\ell=1}^n \mathbf{a}_\ell \nabla_{\mathbf{b}}(L(f)\mathbf{e}_\ell)]_{ij} \neq 0$ if and only if $[v_i, v_j] \in \mathcal{E}(M)$ or $i = j$ for every i, j . As a result, L_2 in (3.20) is stacked by 9 matrices with the same sparsity as L in 3×3 form. Additionally, one can further observe that H in (3.18) is also stacked by 4 matrices with the same sparsity as L in 2×2 form. We summarize this idea as the following theorem.

Theorem 1. H in (3.18) is of identical sparsity to $\mathbf{1}_{2 \times 2} \otimes L$.

Proof. By the Hessian matrix representation of H in (3.18) and the Lemma 2, the proof is obtained. \square

Theorem 1 demonstrates the high sparsity of the Hessian matrix. This property confirms the feasibility of practically solving the large-scale linear system

$$H\mathbf{s} = -\mathbf{g}, \quad (3.24)$$

which inspires us to apply a Newton-type algorithm for solving the optimization problem (3.2). Furthermore, in the representation of H in (3.18), $L_1 - L_2 = \nabla_{\text{vec}(\mathbf{f})} \nabla_{\text{vec}(\mathbf{f})} E_C$ is the Hessian matrix of the conformal energy with respect to $\mathbf{x}, \mathbf{y}, \mathbf{z}$. The term $[\nabla_{\mathbf{x}}^\top, \nabla_{\mathbf{y}}^\top, \nabla_{\mathbf{z}}^\top]^\top$ in (3.18) is the Jacobian matrix of $\mathbf{x}, \mathbf{y}, \mathbf{z}$ with respect to $\boldsymbol{\theta}$ and $\boldsymbol{\phi}$, which is stacked by 3×2 diagonal matrices. The matrix K in (3.18) is also stacked by 2×2 diagonal matrices. These structures are invariant for arbitrary parameterization, and therefore, the sparsity structure of Hessian matrix H is also invariant. Hence, this property is also available on other parameterizations of closed surfaces, including other expressions of spheres and other target regions.

We proceed further to analyze the entries of Hessian matrix H . The entries of L_1 are derived in (3.13) and (3.9), and the entries of K in (3.18) are derived by (3.11a)-(3.11b) and (3.13). We now give the specific derivation for entries of L_2 in (3.18). First, we give the gradients of

$$c_{ij}(f) = -\frac{\langle \mathbf{f}_{ki}, \mathbf{f}_{jk} \rangle}{2|f(T_{ijk})|}, \quad c_{jk}(f) = -\frac{\langle \mathbf{f}_{ij}, \mathbf{f}_{ki} \rangle}{2|f(T_{ijk})|}, \quad c_{ki}(f) = -\frac{\langle \mathbf{f}_{jk}, \mathbf{f}_{ij} \rangle}{2|f(T_{ijk})|}$$

in the triangle $[\mathbf{f}_i, \mathbf{f}_j, \mathbf{f}_k]$, where $c_{ij}(f) := \cot \alpha_{ij}(f)$ as before. Since $c_{ij}(f), c_{jk}(f), c_{ki}(f)$ only relates to vertices $\mathbf{f}_i, \mathbf{f}_j, \mathbf{f}_k$, their gradients with respect to other vertices are 0. The gradients with respect to \mathbf{f}_j are calculated by

$$\frac{\partial}{\partial \mathbf{f}_j} c_{ij}(f) = \frac{1}{|f(T_{ijk})|} \left[-\frac{\partial |f(T_{ijk})|}{\partial \mathbf{f}_j} c_{ij}(f) - \frac{1}{2} \mathbf{f}_{ki} \right], \quad (3.25a)$$

$$\frac{\partial}{\partial \mathbf{f}_j} c_{jk}(f) = \frac{1}{|f(T_{ijk})|} \left[-\frac{\partial |f(T_{ijk})|}{\partial \mathbf{f}_j} c_{jk}(f) + \frac{1}{2} \mathbf{f}_{ki} \right], \quad (3.25b)$$

$$\frac{\partial}{\partial \mathbf{f}_j} c_{ki}(f) = \frac{1}{|f(T_{ijk})|} \left[-\frac{\partial |f(T_{ijk})|}{\partial \mathbf{f}_j} c_{ki}(f) + \frac{1}{2} (\mathbf{f}_{jk} - \mathbf{f}_{ij}) \right], \quad (3.25c)$$

with

$$\frac{\partial |f(T_{ijk})|}{\partial \mathbf{f}_i} = \frac{1}{2} (c_{ij}(f) \mathbf{f}_{ij} - c_{ki}(f) \mathbf{f}_{ki}), \quad (3.26a)$$

$$\frac{\partial |f(T_{ijk})|}{\partial \mathbf{f}_j} = \frac{1}{2} (c_{jk}(f) \mathbf{f}_{jk} - c_{ij}(f) \mathbf{f}_{ij}), \quad (3.26b)$$

$$\frac{\partial |f(T_{ijk})|}{\partial \mathbf{f}_k} = \frac{1}{2} (c_{ki}(f) \mathbf{f}_{ki} - c_{jk}(f) \mathbf{f}_{jk}). \quad (3.26c)$$

The others can be obtained by rotating the subscript i, j, k in turn.

Now, we derive the entries of matrix L_2 in (3.18). Let us consider the block $\sum_{\ell=1}^n \mathbf{a}_\ell \nabla_{\mathbf{b}}(L(f) \mathbf{e}_\ell)$ for $\mathbf{a}, \mathbf{b} = \mathbf{x}, \mathbf{y}, \mathbf{z}$, the (i, j) -th entry of which is

$$\begin{aligned} \left[\sum_{\ell=1}^n \mathbf{a}_\ell \nabla_{\mathbf{b}}(L(f) \mathbf{e}_\ell) \right]_{ij} &= \sum_{\ell=1}^n \mathbf{a}_\ell \frac{\partial}{\partial \mathbf{b}_j} [L(f)]_{i\ell} = \mathbf{a}_i \frac{\partial}{\partial \mathbf{b}_j} [L(f)]_{ii} + \sum_{\ell \in \mathcal{N}(i)} \mathbf{a}_\ell \frac{\partial}{\partial \mathbf{b}_j} [L(f)]_{i\ell} \\ &= \mathbf{a}_i \frac{\partial}{\partial \mathbf{b}_j} \sum_{\ell \in \mathcal{N}(i)} w_{i\ell}(f) - \sum_{\ell \in \mathcal{N}(i)} \mathbf{a}_\ell \frac{\partial}{\partial \mathbf{b}_j} w_{i\ell}(f) \\ &= \sum_{\ell \in \mathcal{N}(i)} \mathbf{a}_{i\ell} \frac{\partial}{\partial \mathbf{b}_j} w_{i\ell}(f). \end{aligned}$$

(i) For $j \neq i$, there are only three vertices $v_j, v_k, v_{k'}$ related to v_i among all adjacent vertices of v_i , as shown in Figure 1. Therefore,

$$\begin{aligned} \left[\sum_{\ell=1}^n \mathbf{a}_\ell \nabla_{\mathbf{b}}(L(f) \mathbf{e}_\ell) \right]_{ij} &= \sum_{\ell \in \{j, k, k'\}} \mathbf{a}_{i\ell} \frac{\partial}{\partial \mathbf{b}_j} w_{i\ell}(f) \\ &= \mathbf{a}_{ik} \frac{\partial}{\partial \mathbf{b}_j} w_{ik}(f) + \mathbf{a}_{ik'} \frac{\partial}{\partial \mathbf{b}_j} w_{ik'}(f) + \mathbf{a}_{ij} \frac{\partial}{\partial \mathbf{b}_j} w_{ij}(f) \\ &= \frac{1}{2} \left[\left(\mathbf{a}_{ij} \frac{\partial}{\partial \mathbf{b}_j} c_{ij}(f) - \mathbf{a}_{ki} \frac{\partial}{\partial \mathbf{b}_j} c_{ki}(f) \right) + \left(\mathbf{a}_{ik'} \frac{\partial}{\partial \mathbf{b}_j} c_{ik'}(f) - \mathbf{a}_{ji} \frac{\partial}{\partial \mathbf{b}_j} c_{ji}(f) \right) \right]. \end{aligned} \quad (3.27)$$

One can see that the terms in the first bracket relate only to triangle T_{ijk} , while the terms in the second bracket relate to triangle $T_{k'ji}$, which are of the same form. This characteristic is also similar to L , whose cotangent weight is $w_{ij} = \frac{1}{2}(c_{ij} + c_{ji})$ with c_{ij}, c_{ji} also relating to T_{ijk} and $T_{k'ji}$, respectively. Hence, we only give the specific representation of the first bracket of (3.27). The second bracket is obtained similarly. By (3.25a)-(3.25c), we have

$$\begin{aligned} &\mathbf{a}_{ij} \frac{\partial}{\partial \mathbf{b}_j} c_{ij}(f) + \mathbf{a}_{ik} \frac{\partial}{\partial \mathbf{b}_j} c_{ki}(f) \\ &= - \frac{1}{2|f(T_{ijk})|} \left[\frac{2\partial |f(T_{ijk})|}{\partial \mathbf{a}_i} \frac{2\partial |f(T_{ijk})|}{\partial \mathbf{b}_j} + (2\mathbf{a}_{ki} \mathbf{b}_{jk} - \mathbf{a}_{jk} \mathbf{b}_{ki}) \right]. \end{aligned} \quad (3.28)$$

(ii) For $j = i$, the related vertices are the whole adjacent vertices of v_i and itself, i.e., $\mathcal{N}(i) \cup \{i\}$. Hence,

$$\begin{aligned} \left[\sum_{\ell=1}^n \mathbf{b}_\ell \nabla_{\mathbf{a}}(L(f) \mathbf{e}_\ell) \right]_{ii} &= \sum_{\ell \in \mathcal{N}(i)} \mathbf{a}_{i\ell} \frac{\partial}{\partial \mathbf{b}_i} w_{i\ell}(f) \\ &= \frac{1}{2} \sum_{\{j, k\} \in S_{\mathcal{E}}(i)} \left(\mathbf{a}_{ij} \frac{\partial}{\partial \mathbf{b}_i} c_{ij}(f) - \mathbf{a}_{ki} \frac{\partial}{\partial \mathbf{b}_i} c_{ki}(f) \right), \end{aligned}$$

where $S_{\mathcal{E}}(i) = \{\{j, k\} \mid j, k \in \mathcal{N}(i), [v_j, v_k] \in \mathcal{E}(M)\}$. Similarly, via the gradient formulas (3.25a)-(3.25c), we have

$$\begin{aligned} &\mathbf{a}_{ij} \frac{\partial}{\partial \mathbf{b}_i} c_{ij}(f) - \mathbf{a}_{ki} \frac{\partial}{\partial \mathbf{b}_i} c_{ki}(f) \\ &= - \frac{1}{2|f(T_{ijk})|} \left[\frac{2\partial |f(T_{ijk})|}{\partial \mathbf{a}_i} \frac{2\partial |f(T_{ijk})|}{\partial \mathbf{b}_i} + \mathbf{a}_{jk} \mathbf{b}_{jk} \right]. \end{aligned} \quad (3.29)$$

We now have derived the entries of matrix $L_1 - L_2$, which is the Hessian matrix of the conformal energy with respect to Cartesian coordinates $[\mathbf{x}, \mathbf{y}, \mathbf{z}]$. The following theorem shows that the nullity of $L_1 - L_2$ is 3.

Theorem 2. $L_1 - L_2$ is a symmetric Laplacian matrix with its null space having orthogonal basis $[\mathbf{1}^\top, \mathbf{0}^\top, \mathbf{0}^\top]^\top$, $[\mathbf{0}^\top, \mathbf{1}^\top, \mathbf{0}^\top]^\top$ and $[\mathbf{0}^\top, \mathbf{0}^\top, \mathbf{1}^\top]^\top$.

Proof. Since $L_1 - L_2$ is the Hessian matrix of the conformal energy with respect to Cartesian coordinates $[\mathbf{x}, \mathbf{y}, \mathbf{z}]$, it is obviously symmetric. By the gradient formulas (3.25a)-(3.25c), it is easily seen that

$$\left(\frac{\partial}{\partial \mathbf{f}_i} + \frac{\partial}{\partial \mathbf{f}_j} + \frac{\partial}{\partial \mathbf{f}_k} \right) c_{ij}(f) = 0.$$

Therefore, by using the representation according to the adjacent vertices, we have

$$\begin{aligned} \sum_{j=1}^n \left[\sum_{\ell=1}^n \mathbf{a}_\ell \nabla_{\mathbf{b}}(L(f)\mathbf{e}_\ell) \right]_{ij} &= \frac{1}{2} \sum_{j \in \mathcal{N}(i)} \mathbf{a}_{ij} \left(\frac{\partial}{\partial \mathbf{b}_i} + \frac{\partial}{\partial \mathbf{b}_j} + \frac{\partial}{\partial \mathbf{b}_k} \right) c_{ij}(f) \\ &\quad - \frac{1}{2} \sum_{j \in \mathcal{N}(i)} \mathbf{a}_{ji} \left(\frac{\partial}{\partial \mathbf{b}_i} + \frac{\partial}{\partial \mathbf{b}_j} + \frac{\partial}{\partial \mathbf{b}_{k'}} \right) c_{ji}(f) = 0, \quad i = 1, 2, \dots, n. \end{aligned}$$

Additionally, by the equality $\mathbf{1}^\top (\nabla_{\mathbf{b}} L(f)\mathbf{e}_\ell) = \nabla_{\mathbf{b}}(\mathbf{1}^\top L(f)\mathbf{e}_\ell) = 0$, we also have

$$\sum_{i=1}^n \left[\sum_{\ell=1}^n \mathbf{a}_\ell \nabla_{\mathbf{b}}(L(f)\mathbf{e}_\ell) \right]_{ij} = \left[\sum_{\ell=1}^n \mathbf{a}_\ell \nabla_{\mathbf{b}}(\mathbf{1}^\top L(f)\mathbf{e}_\ell) \right] \mathbf{e}_j = 0, \quad j = 1, 2, \dots, n.$$

We conclude that the sum of each row and column of $\sum_{\ell=1}^n \mathbf{a}_\ell \nabla_{\mathbf{b}}(L(f)\mathbf{e}_\ell)$ are zero, which guarantees the 3 orthogonal basis of the null space. \square

Finally, we focus on

$$H_2 := \begin{bmatrix} \nabla \mathbf{x}^\top \\ \nabla \mathbf{y}^\top \\ \nabla \mathbf{z}^\top \end{bmatrix} L_2 \begin{bmatrix} \nabla \mathbf{x} \\ \nabla \mathbf{y} \\ \nabla \mathbf{z} \end{bmatrix} = \begin{bmatrix} H_{2,\theta\theta} & H_{2,\theta\phi} \\ H_{2,\phi\theta} & H_{2,\phi\phi} \end{bmatrix}$$

defined in (3.18) and (3.19). The formulas (3.28) and (3.29) show that the entries of L_2 can be rewritten as the inner products of two terms related to \mathbf{a} and \mathbf{b} , respectively. Taking (3.29) as an example, we have

$$\mathbf{a}_{ij} \frac{\partial}{\partial \mathbf{b}_i} c_{ij}(f) + \mathbf{a}_{ik} \frac{\partial}{\partial \mathbf{b}_i} c_{ki}(f) = -\frac{1}{2|f(T_{ijk})|} \left\langle \left[\frac{2\partial|f(T_{ijk})|}{\partial \mathbf{a}_i}, \mathbf{a}_{jk} \right], \left[\frac{2\partial|f(T_{ijk})|}{\partial \mathbf{b}_i}, \mathbf{b}_{jk} \right] \right\rangle,$$

From gradient formulas (3.26a)-(3.26c), we can find that the first and second terms are only associated with \mathbf{a} and \mathbf{b} , respectively. Additionally, (3.28) can also be written as a similar inner product form. Then, since \mathbf{f}_i depends only on (θ_i, ϕ_i) for $i = 1, 2, \dots, n$, the Jacobian matrices of $\mathbf{x}, \mathbf{y}, \mathbf{z}$ with respect to θ, ϕ are diagonal. It is easy to express the products of Jacobian matrices and L_2 . Without loss of generality, we discuss only entry $[H_{2,\theta\phi}]_{ii}$,

$$\begin{aligned} [H_{2,\theta\phi}]_{ii} &= \sum_{\{j,k\} \in S_{\mathcal{E}(i)}} \sum_{\mathbf{a}, \mathbf{b} = \mathbf{x}, \mathbf{y}, \mathbf{z}} \left(\mathbf{a}_{ij} \frac{\partial}{\partial \mathbf{b}_i} c_{ij}(f) - \mathbf{a}_{ki} \frac{\partial}{\partial \mathbf{b}_i} c_{ki}(f) \right) \frac{\partial \mathbf{a}_i}{\partial \theta_i} \frac{\partial \mathbf{b}_i}{\partial \phi_i} \\ &= - \sum_{\{j,k\} \in S_{\mathcal{E}(i)}} \frac{1}{2|f(T_{ijk})|} \sum_{\mathbf{a}, \mathbf{b} = \mathbf{x}, \mathbf{y}, \mathbf{z}} \left\langle \frac{\partial \mathbf{a}_i}{\partial \theta_i} \left[\frac{2\partial|f(T_{ijk})|}{\partial \mathbf{a}_i}, \mathbf{a}_{jk} \right], \frac{\partial \mathbf{b}_i}{\partial \phi_i} \left[\frac{2\partial|f(T_{ijk})|}{\partial \mathbf{b}_i}, \mathbf{b}_{jk} \right] \right\rangle \\ &= - \sum_{\{j,k\} \in S_{\mathcal{E}(i)}} \frac{1}{2|f(T_{ijk})|} \left\langle \sum_{\mathbf{a} = \mathbf{x}, \mathbf{y}, \mathbf{z}} \frac{\partial \mathbf{a}_i}{\partial \theta_i} \left[\frac{2\partial|f(T_{ijk})|}{\partial \mathbf{a}_i}, \mathbf{a}_{jk} \right], \sum_{\mathbf{b} = \mathbf{x}, \mathbf{y}, \mathbf{z}} \frac{\partial \mathbf{b}_i}{\partial \phi_i} \left[\frac{2\partial|f(T_{ijk})|}{\partial \mathbf{b}_i}, \mathbf{b}_{jk} \right] \right\rangle \\ &= - \sum_{\{j,k\} \in S_{\mathcal{E}(i)}} \frac{1}{2|f(T_{ijk})|} \left\langle \frac{\partial \mathbf{f}_i}{\partial \theta_i}^\top \left[\frac{2\partial|f(T_{ijk})|}{\partial \mathbf{f}_i}, \mathbf{f}_{jk} \right], \frac{\partial \mathbf{f}_i}{\partial \phi_i}^\top \left[\frac{2\partial|f(T_{ijk})|}{\partial \mathbf{f}_i}, \mathbf{f}_{jk} \right] \right\rangle. \end{aligned}$$

The partial differential terms in (3.26a)-(3.26c) show that they are the linear combination of \mathbf{f} . Hence, only the sum with respect to $\mathbf{x}, \mathbf{y}, \mathbf{z}$ is necessary, such as

$$\begin{bmatrix} \mathbf{a}_{jk}^i \\ \mathbf{b}_{jk}^i \end{bmatrix} := \left(\frac{\partial \mathbf{f}_i}{\partial (\theta_i, \phi_i)} \right)^\top \mathbf{f}_{jk} = \begin{bmatrix} -\mathbf{y}_i \mathbf{x}_{jk} + \mathbf{x}_i \mathbf{y}_{jk} \\ \mathbf{u}_i \mathbf{x}_{jk} + \mathbf{v}_i \mathbf{y}_{jk} - \mathbf{w}_i \mathbf{z}_{jk} \end{bmatrix}, \quad (3.30a)$$

$$\begin{bmatrix} \mathbf{a}_{ki}^i \\ \mathbf{b}_{ki}^i \end{bmatrix} := \left(\frac{\partial \mathbf{f}_i}{\partial (\theta_i, \phi_i)} \right)^\top \mathbf{f}_{ki} = \begin{bmatrix} -\mathbf{y}_i \mathbf{x}_{ki} + \mathbf{x}_i \mathbf{y}_{ki} \\ \mathbf{u}_i \mathbf{x}_{ki} + \mathbf{v}_i \mathbf{y}_{ki} - \mathbf{w}_i \mathbf{z}_{ki} \end{bmatrix}, \quad (3.30b)$$

$$\begin{bmatrix} \mathbf{a}_{ij}^i \\ \mathbf{b}_{ij}^i \end{bmatrix} := \left(\frac{\partial \mathbf{f}_i}{\partial (\boldsymbol{\theta}_i, \boldsymbol{\phi}_i)} \right)^\top \mathbf{f}_{ij} = \begin{bmatrix} -\mathbf{y}_i \mathbf{x}_{ij} + \mathbf{x}_i \mathbf{y}_{ij} \\ \mathbf{u}_i \mathbf{x}_{ij} + \mathbf{v}_i \mathbf{y}_{ij} - \mathbf{w}_i \mathbf{z}_{ij} \end{bmatrix}. \quad (3.30c)$$

The others are defined similarly by modifying the superscripts and subscripts. Here, \mathbf{a}^i denotes the $\partial \boldsymbol{\theta}_i$ term, and \mathbf{b}^i denotes the $\partial \boldsymbol{\phi}_i$ term. Thus, we have

$$\begin{aligned} \frac{\partial \mathbf{f}_i}{\partial \boldsymbol{\theta}_i} \top \left[\frac{2\partial |f(T_{ijk})|}{\partial \mathbf{f}_i}, \mathbf{f}_{jk} \right] &= \frac{\partial \mathbf{f}_i}{\partial \boldsymbol{\theta}_i} \top [c_{ij}(f) \mathbf{f}_{ij} - c_{ki}(f) \mathbf{f}_{ki}, \mathbf{f}_{jk}] \\ &= [c_{ij}(f) \mathbf{a}_{ij}^i - c_{ki}(f) \mathbf{a}_{ki}^i, \mathbf{a}_{jk}^i]. \end{aligned}$$

We can see that they differ only in $\mathbf{f}.$ and $\mathbf{a}^i, \mathbf{b}^i.$ Hence, the entries of H_2 differ from only those of L_2 with the notations $\mathbf{x}., \mathbf{y}., \mathbf{z}.$ in (3.28) and (3.29) replaced by \mathbf{a}^i and $\mathbf{b}^i.$ Taking $H_{2, \boldsymbol{\theta} \boldsymbol{\phi}}$ as an example, the diagonal and nondiagonal entries are

$$\begin{aligned} [H_{2, \boldsymbol{\theta} \boldsymbol{\phi}}]_{ii} &= - \sum_{\{j,k\} \in \mathcal{S}_{\mathcal{E}(i)}} \frac{1}{4|f(T_{ijk})|} \left[\frac{2\partial |f(T_{ijk})|}{\partial \boldsymbol{\theta}_i} \frac{2\partial |f(T_{ijk})|}{\partial \boldsymbol{\phi}_i} + \mathbf{a}_{jk}^i \mathbf{b}_{jk}^i \right], \\ [H_{2, \boldsymbol{\theta} \boldsymbol{\phi}}]_{ij} &= - \frac{1}{4|f(T_{ijk})|} \left[\frac{2\partial |f(T_{ijk})|}{\partial \boldsymbol{\theta}_i} \frac{2\partial |f(T_{ijk})|}{\partial \boldsymbol{\phi}_j} + (2\mathbf{a}_{ki}^i \mathbf{b}_{jk}^j - \mathbf{a}_{jk}^i \mathbf{b}_{ki}^j) \right] \\ &\quad - \frac{1}{4|f(T_{k'ji})|} \left[\frac{2\partial |f(T_{k'ji})|}{\partial \boldsymbol{\theta}_i} \frac{2\partial |f(T_{k'ji})|}{\partial \boldsymbol{\phi}_j} + (2\mathbf{a}_{ik'}^i \mathbf{b}_{k'j}^j - \mathbf{a}_{k'j}^i \mathbf{b}_{ik'}^j) \right], \end{aligned}$$

respectively, where

$$\frac{\partial |f(T_{ijk})|}{\partial \boldsymbol{\theta}_i} = \frac{1}{2} (c_{ij}(f) \mathbf{a}_{ij}^i - c_{ki}(f) \mathbf{a}_{ki}^i), \quad (3.31a)$$

$$\frac{\partial |f(T_{ijk})|}{\partial \boldsymbol{\phi}_i} = \frac{1}{2} (c_{ij}(f) \mathbf{b}_{ij}^i - c_{ki}(f) \mathbf{b}_{ki}^i). \quad (3.31b)$$

The other entries are obtained similarly by replacing $\partial \mathbf{x}_i, \partial \mathbf{y}_i, \partial \mathbf{z}_i$ and $\mathbf{x}., \mathbf{y}., \mathbf{z}.$ by $\partial \boldsymbol{\theta}_i, \partial \boldsymbol{\phi}_i$ and $\mathbf{a}^i, \mathbf{b}^i$ as in (3.30a)-(3.30c), respectively. Now, we have obtained the entries of Hessian matrix H in (3.18).

Theorem 3. Let $H = \begin{bmatrix} H_{\boldsymbol{\theta} \boldsymbol{\theta}} & H_{\boldsymbol{\theta} \boldsymbol{\phi}} \\ H_{\boldsymbol{\phi} \boldsymbol{\theta}} & H_{\boldsymbol{\phi} \boldsymbol{\phi}} \end{bmatrix}$ with $H_{\boldsymbol{\theta} \boldsymbol{\phi}} = H_{\boldsymbol{\phi} \boldsymbol{\theta}}^\top$. The diagonal and nondiagonal entries of the blocks are

$$\left\{ \begin{array}{l} [H_{\boldsymbol{\theta} \boldsymbol{\theta}}]_{ii} = \sum_{\{j,k\} \in \mathcal{S}_{\mathcal{E}(i)}} \frac{1}{4|f(T_{ijk})|} \left[\left(\frac{2\partial |f(T_{ijk})|}{\partial \boldsymbol{\theta}_i} \right)^2 + (\mathbf{a}_{jk}^i)^2 \right] \\ \quad + \sum_{j \in \mathcal{N}(i)} \tilde{w}_{ij} (\mathbf{x}_i \mathbf{x}_j + \mathbf{y}_i \mathbf{y}_j), \\ [H_{\boldsymbol{\theta} \boldsymbol{\theta}}]_{ij} = \frac{1}{4|f(T_{ijk})|} \left[\frac{2\partial |f(T_{ijk})|}{\partial \boldsymbol{\theta}_i} \frac{2\partial |f(T_{ijk})|}{\partial \boldsymbol{\theta}_j} + (2\mathbf{a}_{ki}^i \mathbf{a}_{jk}^j - \mathbf{a}_{jk}^i \mathbf{a}_{ki}^j) \right] \\ \quad + \frac{1}{4|f(T_{k'ji})|} \left[\frac{2\partial |f(T_{k'ji})|}{\partial \boldsymbol{\theta}_i} \frac{2\partial |f(T_{k'ji})|}{\partial \boldsymbol{\theta}_j} + (2\mathbf{a}_{ik'}^i \mathbf{a}_{k'j}^j - \mathbf{a}_{k'j}^i \mathbf{a}_{ik'}^j) \right] \\ \quad - \tilde{w}_{ij} (\mathbf{x}_i \mathbf{x}_j + \mathbf{y}_i \mathbf{y}_j); \\ [H_{\boldsymbol{\phi} \boldsymbol{\phi}}]_{ii} = \sum_{\{j,k\} \in \mathcal{S}_{\mathcal{E}(i)}} \frac{1}{4|f(T_{ijk})|} \left[\left(\frac{2\partial |f(T_{ijk})|}{\partial \boldsymbol{\phi}_i} \right)^2 + (\mathbf{b}_{jk}^i)^2 \right] \\ \quad + \sum_{j \in \mathcal{N}(i)} \tilde{w}_{ij} (\mathbf{x}_i \mathbf{x}_j + \mathbf{y}_i \mathbf{y}_j + \mathbf{z}_i \mathbf{z}_j), \\ [H_{\boldsymbol{\phi} \boldsymbol{\phi}}]_{ij} = \frac{1}{4|f(T_{ijk})|} \left[\frac{2\partial |f(T_{ijk})|}{\partial \boldsymbol{\phi}_i} \frac{2\partial |f(T_{ijk})|}{\partial \boldsymbol{\phi}_j} + (2\mathbf{b}_{ki}^i \mathbf{b}_{jk}^j - \mathbf{b}_{jk}^i \mathbf{b}_{ki}^j) \right] \\ \quad + \frac{1}{4|f(T_{k'ji})|} \left[\frac{2\partial |f(T_{k'ji})|}{\partial \boldsymbol{\phi}_i} \frac{2\partial |f(T_{k'ji})|}{\partial \boldsymbol{\phi}_j} + (2\mathbf{b}_{ik'}^i \mathbf{b}_{k'j}^j - \mathbf{b}_{k'j}^i \mathbf{b}_{ik'}^j) \right] \\ \quad - \tilde{w}_{ij} (\mathbf{u}_i \mathbf{u}_j + \mathbf{v}_i \mathbf{v}_j + \mathbf{w}_i \mathbf{w}_j); \\ [H_{\boldsymbol{\phi} \boldsymbol{\theta}}]_{ii} = \sum_{\{j,k\} \in \mathcal{S}_{\mathcal{E}(i)}} \frac{1}{4|f(T_{ijk})|} \left[\frac{2\partial |f(T_{ijk})|}{\partial \boldsymbol{\phi}_i} \frac{2\partial |f(T_{ijk})|}{\partial \boldsymbol{\theta}_i} + \mathbf{b}_{jk}^i \mathbf{a}_{jk}^i \right] \\ \quad + \sum_{j \in \mathcal{N}(i)} \tilde{w}_{ij} (\mathbf{v}_i \mathbf{x}_j - \mathbf{u}_i \mathbf{y}_j), \\ [H_{\boldsymbol{\phi} \boldsymbol{\theta}}]_{ij} = \frac{1}{4|f(T_{ijk})|} \left[\frac{2\partial |f(T_{ijk})|}{\partial \boldsymbol{\phi}_i} \frac{2\partial |f(T_{ijk})|}{\partial \boldsymbol{\theta}_j} + (2\mathbf{b}_{ki}^i \mathbf{a}_{jk}^j - \mathbf{b}_{jk}^i \mathbf{a}_{ki}^j) \right] \\ \quad + \frac{1}{4|f(T_{k'ji})|} \left[\frac{2\partial |f(T_{k'ji})|}{\partial \boldsymbol{\phi}_i} \frac{2\partial |f(T_{k'ji})|}{\partial \boldsymbol{\theta}_j} + (2\mathbf{b}_{ik'}^i \mathbf{a}_{k'j}^j - \mathbf{b}_{k'j}^i \mathbf{a}_{ik'}^j) \right] \\ \quad - \tilde{w}_{ij} (\mathbf{v}_i \mathbf{x}_j - \mathbf{u}_i \mathbf{y}_j); \end{array} \right. \quad (3.32)$$

respectively.

Finally, we present a theorem for the proposed algorithm in Section 4, which demonstrates singularity and the corresponding eigenpair of H .

Theorem 4. The null space of H defined in (3.18) has a basis $[\mathbf{1}^\top, \mathbf{0}^\top]^\top$, where $\dim(\mathbf{1}) = \dim(\mathbf{0}) = n$.

Proof. To prove the assertion, we need to indicate only that

$$\mathbf{e}_i^\top H_{\theta\theta}\mathbf{1} = 0, \quad \text{and} \quad \mathbf{e}_i^\top H_{\phi\theta}\mathbf{1} = 0, \quad \text{for } i = 1, 2, \dots, n.$$

We first consider $H_{\phi\theta}$. By (3.32) we have

$$\begin{aligned} \mathbf{e}_i^\top H_{\phi\theta}\mathbf{1} = & \sum_{\{j,k\} \in \mathcal{S}_{\mathcal{E}(i)}} \frac{1}{4|f(T_{ijk})|} \left[\frac{2\partial|f(T_{ijk})|}{\partial\phi_i} \cdot 2 \left(\frac{\partial}{\partial\theta_i} + \frac{\partial}{\partial\theta_j} + \frac{\partial}{\partial\theta_k} \right) |f(T_{ijk})| \right. \\ & \left. + \mathbf{b}_{jk}^i \mathbf{a}_{jk}^i + 2\mathbf{b}_{ki}^i \mathbf{a}_{jk}^j - \mathbf{b}_{jk}^i \mathbf{a}_{ki}^j + 2\mathbf{b}_{ij}^i \mathbf{a}_{jk}^k - \mathbf{b}_{jk}^i \mathbf{a}_{ij}^k \right] \end{aligned} \quad (3.33)$$

It is easy to verify that

$$\mathbf{a}_{ij}^i = \mathbf{a}_{ij}^j, \quad \mathbf{a}_{jk}^j = \mathbf{a}_{jk}^k, \quad \mathbf{a}_{ki}^k = \mathbf{a}_{ki}^i. \quad (3.34)$$

Combining (3.34) with (3.31a), we have

$$\left(\frac{\partial}{\partial\theta_i} + \frac{\partial}{\partial\theta_j} + \frac{\partial}{\partial\theta_k} \right) |f(T_{ijk})| = 0.$$

Hence, by using (3.34) again, (3.33) becomes

$$\begin{aligned} \mathbf{e}_i^\top H_{\phi\theta}\mathbf{1} &= \sum_{\{j,k\} \in \mathcal{S}_{\mathcal{E}(i)}} \frac{1}{4|f(T_{ijk})|} \left[\mathbf{b}_{jk}^i \mathbf{a}_{jk}^i + 2\mathbf{b}_{ki}^i \mathbf{a}_{jk}^j - \mathbf{b}_{jk}^i \mathbf{a}_{ki}^j + 2\mathbf{b}_{ij}^i \mathbf{a}_{jk}^k - \mathbf{b}_{jk}^i \mathbf{a}_{ij}^k \right] \\ &= \sum_{\{j,k\} \in \mathcal{S}_{\mathcal{E}(i)}} \frac{1}{4|f(T_{ijk})|} \mathbf{b}_{jk}^i \left(\mathbf{a}_{ij}^i + \mathbf{a}_{jk}^j + \mathbf{a}_{ki}^k \right) = 0. \end{aligned}$$

Similarly, we also have $\mathbf{e}_i^\top H_{\theta\theta}\mathbf{1} = 0$. Notably, $\mathbf{e}_i^\top H_{\phi\phi}\mathbf{1} \neq 0$. Therefore, the theorem is proved. \square

Remark 2. Geometrically, the one-dimensional null space of H reveals that the conformal energy is invariant up to a rotation along the latitude, while that along the longitude is not characterized, since it is not linearly related to ϕ .

4 Hessian-Based Trust Region Algorithm

In this section, we develop an HBTR algorithm to minimize the conformal energy for the computation of the conformal map from a closed surface of genus-0 to a unit sphere. Here, we review the optimization problem,

$$\min E_C(\boldsymbol{\theta}, \boldsymbol{\phi}) := \frac{1}{2} \langle D(f)\mathbf{f}, \mathbf{f} \rangle, \quad \mathbf{f} = [\cos \boldsymbol{\theta} \odot \sin \boldsymbol{\phi}, \sin \boldsymbol{\theta} \odot \sin \boldsymbol{\phi}, \cos \boldsymbol{\phi}]. \quad (4.1)$$

We loosen the box constraint $(\boldsymbol{\theta}, \boldsymbol{\phi}) \in [0, 2\pi]^n \times [0, \pi]^n$ and consider (4.1) as an unconstrained problem. In Section 3, the gradient vector and Hessian matrix of $E_C(\boldsymbol{\theta}, \boldsymbol{\phi})$ are derived in (3.14) and Theorem 3, respectively. The sparsity of the Hessian matrix shown in Theorem 1 guarantees the feasibility of fast computation associated with H . Specifically, we solve the large-scale sparse linear system to obtain the Newton direction: $H\mathbf{s} = -\mathbf{g}$ as in (3.24). As Theorem 4 demonstrated, H is singular, and the general solution can be expressed as a spherical solution with arbitrary rotation along latitude according to Remark 2. Therefore, we fix the first entry of \mathbf{s} and let

$$H = \begin{bmatrix} h_{11} & \mathbf{h}_1^\top \\ \mathbf{h}_1 & \hat{H} \end{bmatrix}, \quad \mathbf{s} = \begin{bmatrix} 0 \\ \hat{\mathbf{s}} \end{bmatrix}, \quad \mathbf{g} = \begin{bmatrix} g_1 \\ \hat{\mathbf{g}} \end{bmatrix}.$$

Then, we solve the linear system

$$\hat{H}\hat{\mathbf{s}} = -\hat{\mathbf{g}}. \quad (4.2)$$

It is easy to verify that $H\mathbf{s} = -\mathbf{g}$ holds for $\mathbf{s} = [0, \hat{\mathbf{s}}^\top]^\top$. Geometrically, this approach means that the longitude of the first vertex always remains invariant and that meaningless rotation of the sphere is avoided during the iteration.

Remark 3. H can be rearranged from $L \otimes \mathbf{1}_{2 \times 2}$ to $\mathbf{1}_{2 \times 2} \otimes L$. The rearranged matrix is constructed by the 2×2 block in L form such that the block LU decomposition is appropriate for the fast computation of the linear system (4.2).

Therefore, it is natural to use the Newton-type method to solve the optimization problem (4.1). However, the pure Newton method is insufficient for solving the optimization problem directly because the Newton method is well known to have local quadratic convergence. Unfortunately, it is almost impractical to directly seek an initial guess sufficiently close to the ideal solution for (4.1), especially when facing surfaces with high-curvature regions or complicated shapes. Additionally, the conformal energy of (4.1) with respect to $(\boldsymbol{\theta}, \boldsymbol{\phi})$ is nonconvex and nonlinear. Hence, the quadratic convergence generally disappears at the beginning of iterations, and it might take much time to reach the neighborhood with quadratic convergence via the Newton step. Moreover, importantly, the Hessian matrix H is not uniformly positive semidefinite; that is, H may be indefinite at some points $(\boldsymbol{\theta}, \boldsymbol{\phi})$. Indeed, negative curvature occurs frequently during iteration in practical experiments. Consequently, it is possible that the Newton direction may not be a descent direction.

To overcome this drawback, we introduce the negative gradient direction, which is a descent direction. More specifically, we search the trial step \mathbf{d} from the 2D subspace spanned by the Newton direction \mathbf{s} and the gradient direction \mathbf{g} . If \mathbf{s} is not a descent direction, it is a negative curvature direction, which is still beneficial information for the choice of descent direction. Moreover, there must be a descent direction in this 2D subspace since $-\mathbf{g} \in \text{span}(\mathbf{s}, \mathbf{g})$. When the iterative point is in the convergence neighborhood, the Newton direction guarantees the quadratic convergence of the algorithm. We utilize the trust region method to search the trial step from $\text{span}(\mathbf{s}, \mathbf{g})$. In other words, during each iterative step, we consider the trust region subproblem proposed by Shultz et al. [43]

$$\begin{aligned} \min \quad & \mathbf{d}^\top H \mathbf{d} + \mathbf{g}^\top \mathbf{d} \\ \text{s.t.} \quad & \|\mathbf{d}\| \leq \Delta, \mathbf{d} \in \text{span}(\mathbf{s}, \mathbf{g}), \end{aligned} \quad (4.3)$$

where Δ is the trust region radius. The 2D optimization problem (4.3) is easy to solve and costs less time. The global and local convergence of the trust region method with subproblem (4.3) has been proven by [43], and the practical experiment has been verified later in [13].

For the error measurement, it is worth noting that $E_C(\boldsymbol{\theta}, \boldsymbol{\phi})$ is a periodic function. Since we loosen the box constraint $(\boldsymbol{\theta}, \boldsymbol{\phi}) \in [0, 2\pi]^n \times [0, \pi]^n$, $(\boldsymbol{\theta}, \boldsymbol{\phi})$ might move larger than 2π , while the vertices on the sphere move much less. Hence, it is inappropriate to check the length of step \mathbf{d} . Inspired by [47], we adopt the optimal rotation and measure the error with

$$\delta^{(k)} = \min_{R \in SO(3)} \left\| \mathbf{f}^{(k+1)} - \mathbf{f}^{(k)} R \right\|^2, \quad (4.4)$$

where $SO(3) = \{R \in \mathbb{R}^{3 \times 3} \mid R^\top R = I, \det(R) = 1\}$ and $\mathbf{f}^{(k)}$ are the vertices on the sphere at the k -th iteration. The error measurement eliminates the error from rotation. In addition, it avoids the miscalculation caused by the periodicity of $E_C(\boldsymbol{\theta}, \boldsymbol{\phi})$.

We summarize the proposed Hessian-based trust region (HBTR) algorithm for the optimization problem (4.1).

Remark 4. Similar to the disk parameterization in [47], the bijectivity of the resulting map can almost be guaranteed under the spherical coordinate representation. If not, the folding triangles can be removed by the mean value coordinate [24].

5 Numerical Experiments

In this section, we describe the numerical performance of our proposed HBTR method for spherical conformal parameterization on several triangulation models. All experimental programs are executed in MATLAB R2021a on a personal computer with a 2.50 GHz CPU and 64 GB RAM. Most of the triangulation models are taken from AIM@SHAPE shape repository [2], ALICE [1], Gu's personal website [7], the Stanford 3D scanning repository [5], Human Connectome Project [4], and TurboSquid

Algorithm 1 HBTR for Spherical CEM Problem

Require: Triangulation M with vertices $\{v_i, i = 1, 2, \dots, n\}$, tolerance ε .

Ensure: $\mathbf{f} \in \mathbb{R}^{n \times 3}$ inducing the conformal map f as in (3.1).

- 1: Set $k = 0$ and $\delta^{(0)} = +\infty$.
- 2: Compute the initial guess \mathbf{f} and the corresponding conformal energy $E_C^{(0)}$ in (3.3).
- 3: **while** $\delta > \varepsilon$ **do**
- 4: Compute the gradient vector \mathbf{g} and the Hessian matrix H by (3.14) and Theorem 3.
- 5: Solve the linear system $\hat{H}\hat{\mathbf{s}} = -\hat{\mathbf{g}}$ via block LU decomposition to get the Newton direction \mathbf{s} .
- 6: Solve the trust region subproblem (4.3) to get the trial step \mathbf{d} .
- 7: Let $E \leftarrow E_C((\boldsymbol{\theta}, \boldsymbol{\phi}) + \mathbf{d})$. If $E_C^{(k)} > E$, set $k \leftarrow k + 1$ and update

$$(\boldsymbol{\theta}, \boldsymbol{\phi}) \leftarrow (\boldsymbol{\theta}, \boldsymbol{\phi}) + \mathbf{d},$$

$$E_C^{(k)} \leftarrow E.$$

- 8: Compute the error $\delta^{(k)}$ by (4.4) and tune the trust region radius Δ .
 - 9: **end while**
-

[6]. The triangulations of brain cortical surfaces are generated from BraTS datasets [11] via library JIGSAW [20, 19, 18, 21, 17] and toolbox Iso2Mesh [23, 44, 8]. From the abovementioned benchmarks, we take the triangulation models for experiments as shown in Figure 2 and present their basic information for numbers of vertices and faces in Table 1. Notably, no folding occurs on the 8 models by HBTR. We apply the SCEM algorithm proposed in [48] for the initial guess in the experiments. Among the vast experiments, the SCEM can stably provide a great initial guess in a very short time, which is appropriate for the HBTR algorithm.

Mesh	#V	#F	Mesh	#V	#F
Apple	17839	35674	Fandisk	6475	12946
Arnold	14530	29056	Horse	21013	42022
Brain	32160	64316	Planck	51108	102212
Bunny	55684	111364	Venus	14303	28602

Table 1: The features of triangulation models with $\#V$ and $\#F$ being the number of vertices and triangle faces, respectively.

5.1 Convergence behavior and conformal distortion

We first present the convergence behavior of the proposed Algorithm 1. Figure 3 shows the relationship between the number of iterations k and conformal energy $E_C^{(k)}$, the infinity norm of gradient $\|\mathbf{g}^{(k)}\|_\infty$ and the error $\delta^{(k)}$ by Algorithm 1 for models in Figure 2. As shown, the conformal energy $E_C^{(k)}$ with the scale on the right decreases linearly first. Meanwhile, $\|\mathbf{g}^{(k)}\|_\infty$ and $\delta^{(k)}$ with the scale on the left remain stable within a range. At this moment, the gradient and Newton directions are utilized for the trial step. Then, $E_C^{(k)}$ tends to level off, while $\|\mathbf{g}^{(k)}\|_\infty$ and $\delta^{(k)}$ descend sharply. More specifically, $\|\mathbf{g}^{(k)}\|_\infty$ becomes 10^{-10} on most of the models when the iteration loops terminate, implying that the iteration stops at a critical point and the algorithm converges. Moreover, $\delta^{(k)}$ descends in quadratic order. Taking *Brain* as an example, we have

$$\delta^{(25)} = 7.4 \times 10^{-4}, \quad \delta^{(26)} = 9.3 \times 10^{-6}, \quad \delta^{(27)} = 5.9 \times 10^{-10}.$$

Obviously, it shows the quadratic convergence of the HBTR algorithm.

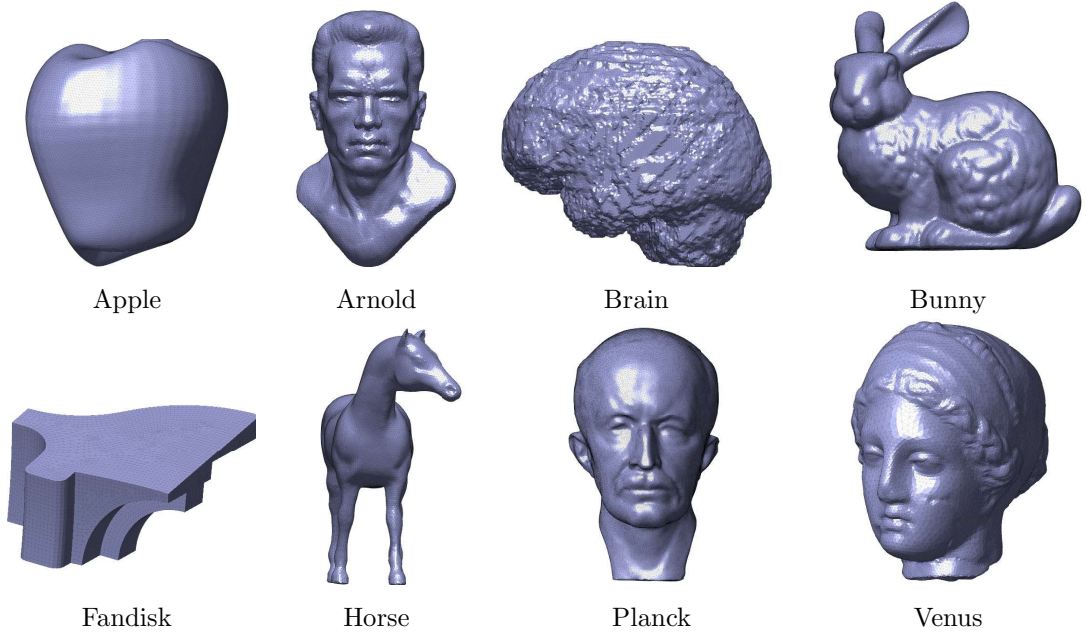


Figure 2: The triangulation models for the experiments.

Figures 4 and 5 present the histograms of absolute angle distortion (degree) of each angle, denoted as $|\alpha_{jk} - \alpha_{jk}(f)|$ for v_i in T_{ijk} , and Beltrami coefficients μ [15] of triangular faces, respectively. If $|\mu| = 0$, the map f is conformal. The subplots in the upper right of each histogram are the front and back of the angle distortion distributions/Beltrami coefficient distributions on the resulting unit spheres, respectively. One can see that most of angle distortions are less than 5 degrees and most of Beltrami coefficients are less than 0.1 as well, guaranteeing the conformal performance of the HBTR algorithm. Angle distortion has similar performance to the Beltrami coefficient. Furthermore, Figure 6 shows the absolute value of the discrete Gauss curvature $|\kappa|$, the average angle distortion ϵ_α and the average of the norm of the Beltrami coefficient $|\overline{\mu}|$ at each vertex for the models *Arnold*, *Brain*, *Fandisk* and *Horse*, denoted as

$$\begin{aligned}\kappa(v_i) &= 2\pi - \sum_{\{j,k\} \in S_{\mathcal{E}}(i)} \alpha_{jk}, \\ \epsilon_\alpha(v_i) &= \frac{1}{|\mathcal{N}(i)|} \sum_{\{j,k\} \in S_{\mathcal{E}}(i)} |\alpha_{jk} - \alpha_{jk}(f)|, \\ |\overline{\mu}|(v_i) &= \frac{1}{|\mathcal{N}(i)|} \sum_{T_{ijk} \ni i} |\mu(T_{ijk})|,\end{aligned}$$

where $|\mathcal{N}(i)|$ is the number of adjacent vertices of v_i and $\mu(T_{ijk})$ is the Beltrami coefficient on triangle T_{ijk} . We approximately find $|\overline{\mu}| \propto \epsilon_\alpha \propto \sqrt{|\kappa|}$ in these 4 models except *Brain*, which approximately satisfies $|\overline{\mu}| \propto \epsilon_\alpha \propto |\kappa|$. The figures are plotted according to the relationships. The textures illustrate the high similarity of high curvatures, large angle distortions and large Beltrami coefficient distributions. In other words, the large angle distortion and the large Beltrami coefficient regions are mainly at those with high curvatures, such as the ears, eyes and nose of *Arnold*, corners of *Fandisk*, and ears and legs of *Horse*. The small angle distortion and small Beltrami coefficient regions are roughly at those with low curvature. Therefore, the HBTR performs relatively poorly at vertices with high curvature, which is an issue in our future work. Additionally, the angle distortion and the Beltrami coefficient have diffusion trends. Taking *Fandisk* as an example, high-curvature regions are on corners and edges, and the curvatures in other regions are mostly 0. Furthermore, the angle distortions and the Beltrami coefficients diffuse from the corners to the adjacent regions gradually. These phenomena also occur in the other models, which are not shown.

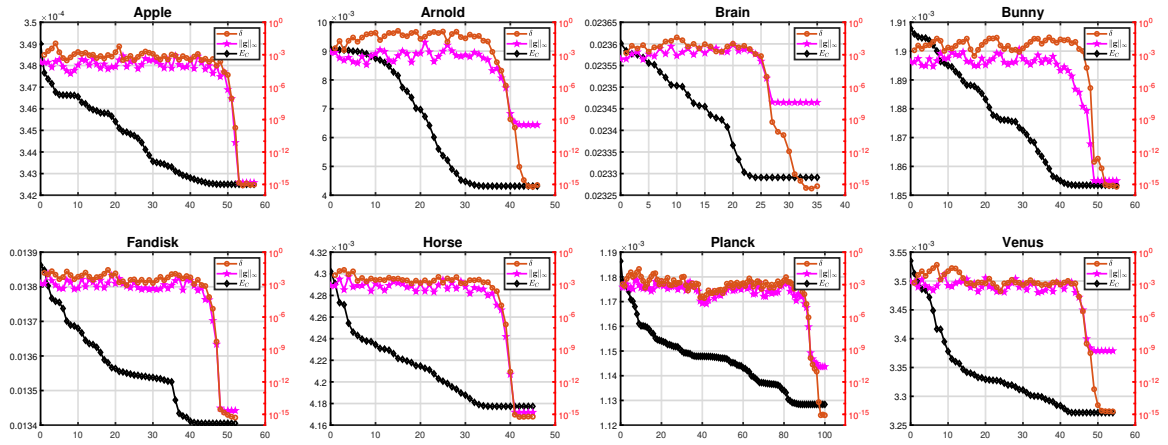


Figure 3: The relationship between the number of iterations k and the conformal energy $E_C^{(k)}$, the infinity norm of gradient $\|\mathbf{g}^{(k)}\|_\infty$ and the error $\delta^{(k)}$ by Algorithm 1. The x -axes represent the number of iterations. The left y -axes represent the conformal energies, and the right y -axes represent infinity norms of gradient and errors, respectively.

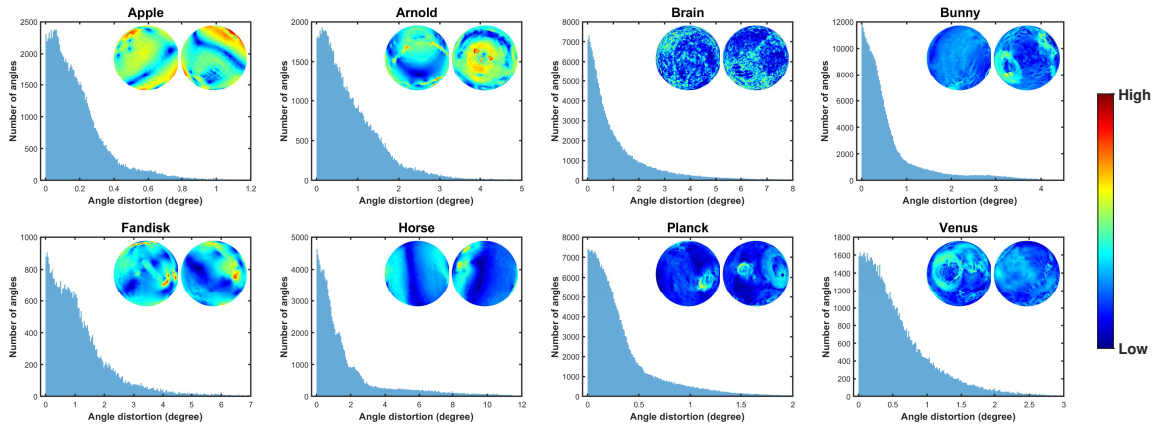


Figure 4: Histograms of angle distortions on triangulation models.

5.2 Comparison with state-of-the-art algorithms

In this subsection, we compare the accuracy of the proposed HBTR algorithm with that of two state-of-the-art algorithms for spherical conformal parameterization, namely, FLASH [15] and the SCEM [48]. The algorithm FLASH, simply put, via the stereographic projection, applies the composition of two quasi-conformal maps to construct the ideal conformal map, which is not an iterative algorithm. The MATLAB program of FLASH is obtained from Choi’s website [3]. The SCEM algorithm, as mentioned in Section 2, adopts the north-south hemisphere alternating iteration to compute the conformal map. The maximum number of iterations of the HBTR and SCEM is 500. The loop termination condition of SCEM is that the difference between the conformal energies of two consecutive iteration steps is less than 10^{-9} . For the HBTR algorithm, we set $\varepsilon = 10^{-9}$, as in Figure 3, which guarantees convergence.

Table 2 shows the comparison of conformal energies between FLASH, SCEM and HBTR. We can see that the conformal energies by HBTR are smallest among all models. In the view of angle distortions, it is observed that the HBTR algorithm has well performance for 50-th percentile and 75-th percentile as FLASH and SCEM. In addition, among the 8 testing examples, FLASH, SCEM and HBTR did not produce foldings for spherical conformal maps.

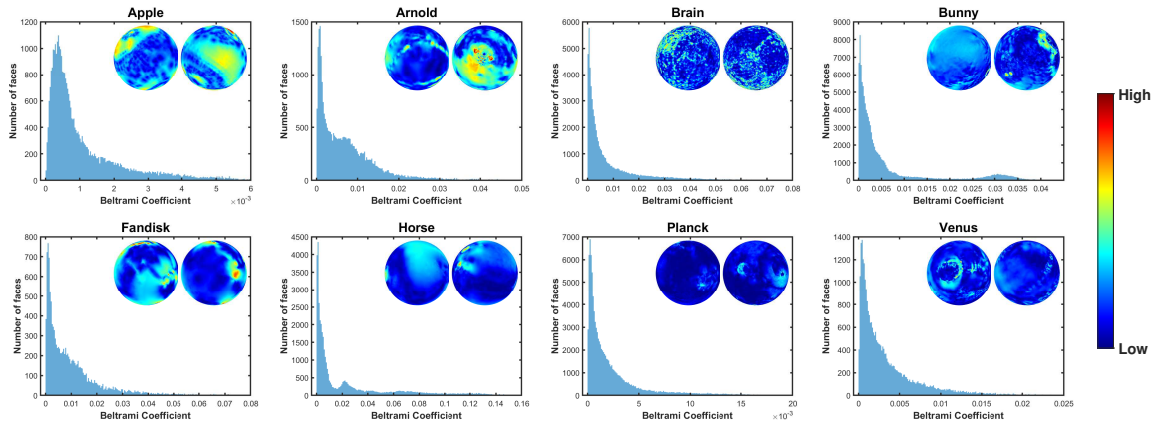


Figure 5: Histograms of the Beltrami coefficients in the triangulation models.

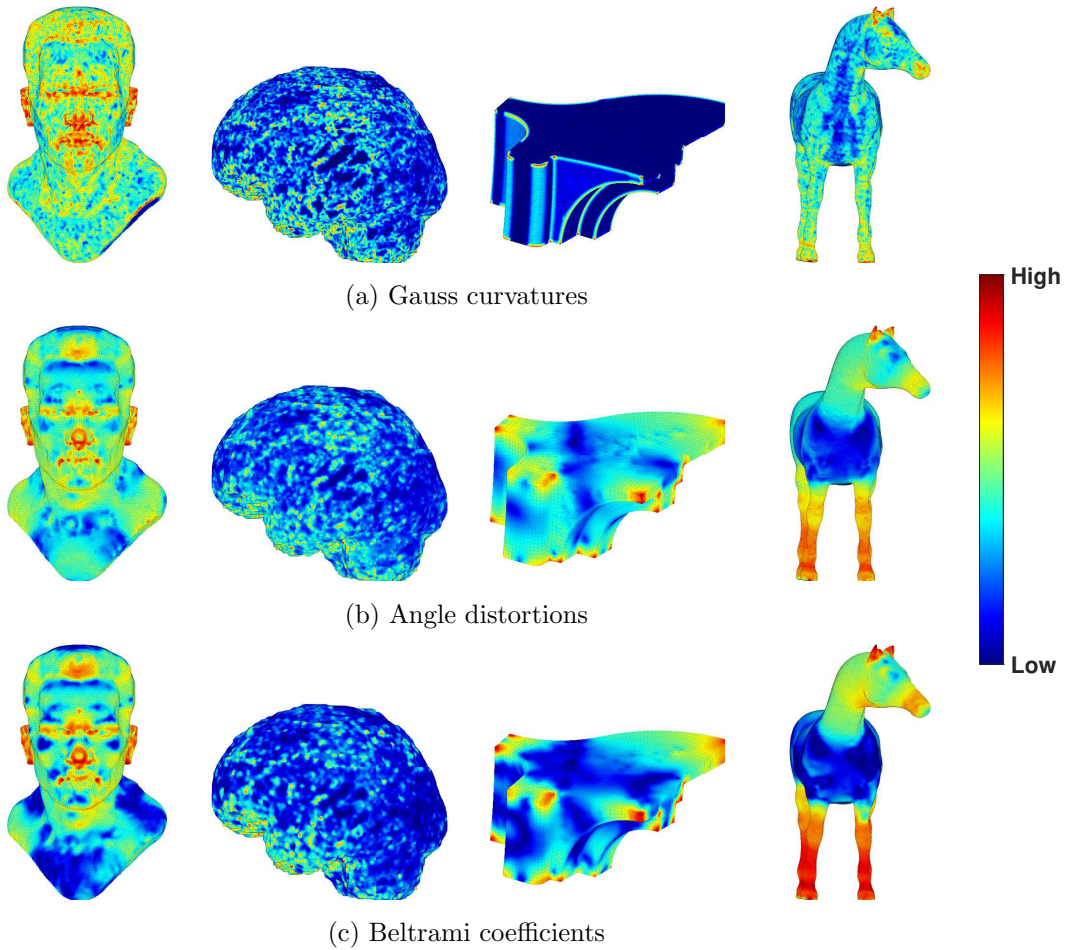


Figure 6: (a) Gauss curvature distributions (top), (b) angle distortion distributions, and (c) Beltrami coefficient distributions (bottom) for models *Arnold*, *Brain*, *Fandisk* and *Horse*.

Mesh	Conformal Energy			Angle Distortion					
				50-th percentile			75-th percentile		
	FLASH[15]	SCEM[48]	HBTR	FLASH[15]	SCEM[48]	HBTR	FLASH[15]	SCEM[48]	HBTR
Apple	3.74e-04	3.49e-04	3.43e-04	0.162	0.156	0.153	0.280	0.268	0.264
Arnold	7.82e-03	9.07e-03	4.32e-03	0.676	0.675	0.659	1.232	1.173	1.233
Brain	2.69e-02	2.36e-02	2.33e-02	0.821	0.729	0.729	1.849	1.694	1.694
Bunny	1.93e-03	1.90e-03	1.85e-03	0.343	0.339	0.363	0.759	0.746	0.735
Fandisk	3.50e-02	1.39e-02	1.34e-02	1.071	0.936	0.936	1.974	1.646	1.640
Horse	4.58e-03	4.30e-03	4.18e-03	1.027	1.020	1.010	2.292	2.283	2.283
Planck	1.71e-03	1.19e-03	1.13e-03	0.311	0.245	0.231	0.578	0.457	0.446
Venus	6.66e-03	3.54e-03	3.27e-03	0.666	0.453	0.442	1.186	0.831	0.821

Table 2: Comparison of conformal energies and angle distortions between FLASH, SCEM and HBTR.

5.3 Convergence behavior of the discrete scheme

In this subsection, we check the numerical convergence of the discrete conformal energy of the resulting map to the continuous energy in (2.1). We consider two ellipsoids with semiaxis lengths of (1.1, 1, 0.9) and (2.0, 1, 0.3) and generate triangular meshes with different resolutions. The basic information of the meshes is in Table 3, where h represents the maximum diameter of triangles in the mesh. Then, we use FLASH, SCEM and HBTR to compute conformal parameterizations. The conformal energies, means and SDs of angle distortion are used to measure the conformal distortion of the algorithms. Figure 7 shows the relationship between the measurements and h . The x -axis represents h and y -axis represents the conformal energy, mean and SD of angle distortion, respectively. We can see that the conformal energy, mean and SD do not stably decrease as h decreases for FLASH, while $E_C = O(h^2)$ and angle distortions are linearly related to h for SCEM and HBTR. Specifically, as $h \rightarrow \frac{1}{2}h$, $E_C \rightarrow \frac{1}{4}E_C$, the means and SDs are reduced by half. Therefore, SCEM and HBTR are robust in the respective of convergence of the discrete scheme. The conformal energies, means and SDs are lowest for HBTR compared with those of FLASH and SCEM, demonstrating the robustness and accuracy of HBTR.

	#V	642	2562	10242	40962	163842	655362
	#F	1280	5120	20480	81920	327680	1310720
h	(1.1, 1, 0.9)	0.1796	0.0901	0.0451	0.0226	0.0113	0.0056
	(2.0, 1, 0.3)	0.3192	0.1607	0.0806	0.0403	0.0202	0.0101

Table 3: The ellipsoids meshes for checking the convergence of the discrete scheme.

5.4 Removal of folding triangles

HBTR does not necessarily guarantee the bijectivity of the resulting map; that is, folding triangles may occur in the image region \mathbb{S}^2 . In this subsection, we apply a postprocessing method, named mean value coordinates [24], to remove the folding triangles. Let L_{MV} be a Laplacian matrix defined as

$$[L_{MV}]_{ij} = \begin{cases} -w_{MV,ij} & \text{if } i \neq j, [v_i, v_j] \in \mathcal{E}(M), \\ \sum_{k \in \mathcal{N}(i)} w_{MV,ik} & \text{if } i = j, \\ 0 & \text{if } [v_i, v_j] \notin \mathcal{E}(M), \end{cases} \quad (5.1)$$

with

$$w_{MV,ij} = \frac{\tan(\alpha_{jk}/2) + \tan(\alpha_{k'j}/2)}{\|v_{ij}\|},$$

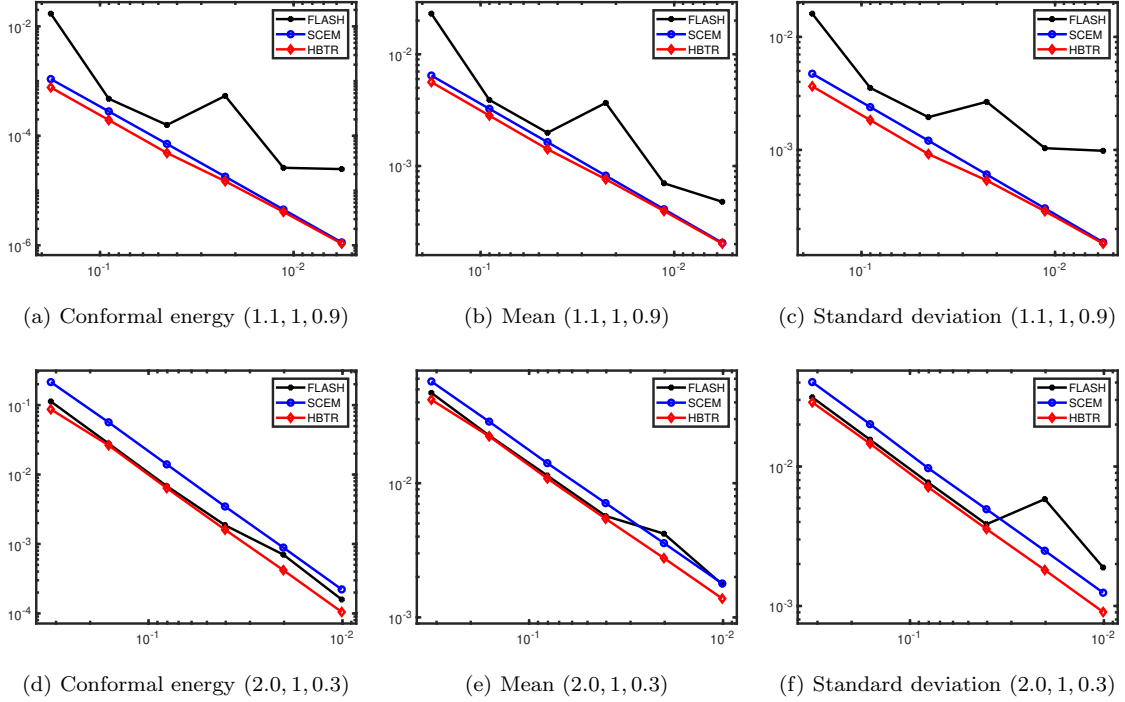


Figure 7: The relationship between conformal energy, mean and standard deviation of angle distortion and h of algorithms FLASH, SCEM and HBTR for 2 ellipsoids. The figures from the top row to the bottom row are for ellipsoids (1.1, 1, 0.9) and (2.0, 1, 0.3), respectively.

where α_{jk} and $\alpha_{k'j}$ are the angles opposite to vertex v_i in triangles T_{ijk} and $T_{k'ji}$, respectively, as shown in Figure 1a. The postprocessing method is concluded in Algorithm 2.

Unlike L in conformal energy in (3.3), L_{MV} is not symmetric. However, its weights w_{MV} must be positive. Therefore, this approach can guarantee the bijectivity of the modified map. We present 2 examples, the resulting maps of which by HBTR are not bijective. Then, we use Algorithm 2 to remove the folding triangles. Table 4 shows the conformal energies, angle distortions and the number of folding triangles before and after the removal. The conformal energies decrease slightly, and the angle distortions are almost unchanged, while the folding triangles disappear.

Mesh	$\#V$	$\#F$	Conformal energy	Mean of angle distortion	$\#\text{folding}$
Bimba	502575	1005146	1.132e-3 / 1.113e-3	5.328e-3 / 5.328e-3	24 / 0
RightBrain	163842	327680	2.806e-2 / 2.799e-2	2.252e-2 / 2.252e-2	34 / 0

Table 4: The result of postprocessing for removing the folding triangles. The left and right of '/' are the values before and after the postprocessing, respectively.

6 Application to surface registrations

Given a fixed surface M_0 and a series of moving surfaces $M_t, t = 1, 2, \dots$, surface registration aims to find bijective maps from the moving surfaces to the fixed surface. It is broadly applied in computer vision and medical imaging. The goal of surface registration is to transform surfaces from different sources into one coordinate system. Therefore, the registration should ensure that the predominant features in the fixed surface correspond to those in the target surfaces, which are often expressed as landmarks in practical applications. It is generally not easy to manage the registration because of the complicated structure of surfaces. With the help of parameterization, we can transform the closed

Algorithm 2 Mean value coordinates for removing folding triangles

Require: Triangulation M with vertices $\{v_i, i = 1, 2, \dots, n\}$, and $\mathbf{f} \in \mathbb{R}^{n \times 3}$ obtained by Algorithm 1.

Ensure: $\mathbf{f} \in \mathbb{R}^{n \times 3}$ inducing the conformal map f as in (3.1) guaranteeing the bijectivity.

- 1: Generate Laplacian matrix L_{MV} defined in (5.1).
- 2: Search the folding triangles in $f(M)$. Let $\mathbf{I} = \{i \mid T_{ijk} \text{ is a folding triangle.}\}$ be the index set of vertices contained in the folding triangles and $\mathbf{0} = \{1, 2, \dots, n\} \setminus \mathbf{I}$.
- 3: **while** $\mathbf{I} \neq \emptyset$ **do**
- 4: Select the face center of an unfolding triangle as north pole and perform the stereographic projection $\Pi(\mathbf{f}) \rightarrow \mathbf{h}$.
- 5: Update the vertices $\mathbf{h}_{\mathbf{I}}$ by solving the linear system,

$$[L_{MV}]_{\mathbf{I}\mathbf{I}} \mathbf{h}_{\mathbf{I}} = -[L_{MV}]_{\mathbf{I}\mathbf{0}} \mathbf{h}_{\mathbf{0}}. \quad (5.2)$$

- 6: Perform the inverse stereographic projection $\Pi^{-1}(\mathbf{h}) \rightarrow \mathbf{f}$ and update \mathbf{I} and $\mathbf{0}$.

7: **end while**

fixed surface M_0 into a unit sphere \mathbb{S}^2 via conformal map f_0 and then register the moving surfaces to the obtained unit sphere \mathbb{S}^2 via registration map $f_{reg,t}$. As a result, the map $\tilde{f}_{reg,t} = f_0^{-1} \circ f_{reg,t}$ is the registration map from M_t to M_0 . To obtain $f_{reg,t}$, we consider the optimization problem

$$\min E_B(\boldsymbol{\theta}, \boldsymbol{\phi}) := E_C(\boldsymbol{\theta}, \boldsymbol{\phi}) + \lambda E_{reg}(\boldsymbol{\theta}, \boldsymbol{\phi}), \quad (6.1)$$

where E_{reg} is the registration loss and λ is its parameter. The representation of E_{reg} depends on the expression of predominant features. The most common representation is the landmark-based registration

$$E_{reg} = \frac{1}{2|S_L|} \sum_{i \in S_L} \|\mathbf{f}_{t,i} - \mathbf{f}_{0,i}\|_F^2, \quad (6.2)$$

where $\mathbf{f}_{t,i}$ are the feature vertices on surface M_t and S_L and $|S_L|$ are the indices set and the number of the landmark vertices, respectively. Landmark-based registration aims to align the landmark vertices such that the features of the surfaces are also aligned.

The conformal energy term guarantees the conformality of the map, while the registration loss term aligns the features of the surfaces. Therefore, the combination of the conformal energy and the registration loss results in a conformal (as possible) registration map. The conformal registration map is an elastic registration and preserves the local shape of the surface, which is widely used in the field of medical imaging. For the optimization problem (6.1), it is easy to derive the gradient vector and Hessian matrix of registration loss generally. Benefiting from their simple representations, we can also utilize HBTR to solve it. Moreover, the conformal energy is invariant up to arbitrary rotation on \mathbb{S}^2 . Therefore, we introduce an optimal rotation to further decrease the registration loss. Based on Algorithm 1, we present the following spherical conformal registration algorithm.

To present the registration performance of our method, we take 5 right brain cortex meshes $RBrain0 - RBrain4$ from the Human Connectome Project [4] as an example, which are shown in the top row of Figure 8, in which the regions in different colors represent different parts of the brain. We select 3 landmark curves for each brain, which are in red, green and cyan, respectively, as shown in the top row of Figure 8. We select $RBrain0$ as the fixed surface and register $RBrain1 - RBrain4$ to it. The parameter λ in (6.1) is chosen as 1, 5, 10 successively. The middle row shows the resulting spheres by solving the registration problem (6.1) with the landmark curves, respectively, with $\lambda = 5$. The bottom row shows the corresponding registered brains. The high similarity of the landmark curves between the fixed brain and registered brains illustrates the well performance of our method. Notably, all registration maps are bijective. Table 5 presents their conformal energies, angle distortions and

Algorithm 3 HBTR for spherical conformal registration

Require: Fixed surface M_0 and moving surface M_t with landmarks, registration parameter λ , tolerance ε .

Ensure: The conformal registration map $\tilde{f}_{reg,t}$.

- 1: Compute the spherical conformal map of M_0 by Algorithm 1, denoted as f_0 .
- 2: Set $k = 0$ and $\delta^{(0)} = +\infty$.
- 3: Compute the initial guess \mathbf{f} of M_t .
- 4: Compute the optimal rotation R according to the landmarks, update $\mathbf{f} \leftarrow \mathbf{f}R$ and compute the corresponding term $E_B^{(0)}$ in (6.1).
- 5: **while** $\delta > \varepsilon$ **do**
- 6: Compute gradient vector \mathbf{g} and Hessian matrix H of (6.1).
- 7: Solve the linear system $H\mathbf{s} = -\mathbf{g}$ via block LU decomposition.
- 8: Solve the trust region subproblem (4.3) to get the trial step \mathbf{d} .
- 9: Compute the optimal rotation R according to the landmarks to update \mathbf{d} .
- 10: Let $E \leftarrow E_B((\boldsymbol{\theta}, \boldsymbol{\phi}) + \mathbf{d})$. If $E_B^{(k)} > E$, set $k \leftarrow k + 1$ and update

$$\begin{aligned}(\boldsymbol{\theta}, \boldsymbol{\phi}) &\leftarrow (\boldsymbol{\theta}, \boldsymbol{\phi}) + \mathbf{d}, \\ E_B^{(k)} &\leftarrow E.\end{aligned}$$

- 11: Compute the error $\delta^{(k)}$ by (4.4) and tune the trust region radius Δ .

12: **end while**

- 13: Let $\mathbf{f}_{reg,t} = [\cos \boldsymbol{\theta} \odot \sin \boldsymbol{\phi}, \sin \boldsymbol{\theta} \odot \sin \boldsymbol{\phi}, \cos \boldsymbol{\phi}]$. Compute $\tilde{f}_{reg,t} = f_0^{-1} \circ f_{reg,t}$, which is the registration map of M_t .
-

registration losses. As the parameter λ increases, the conformal energies and angle distortions remain low.

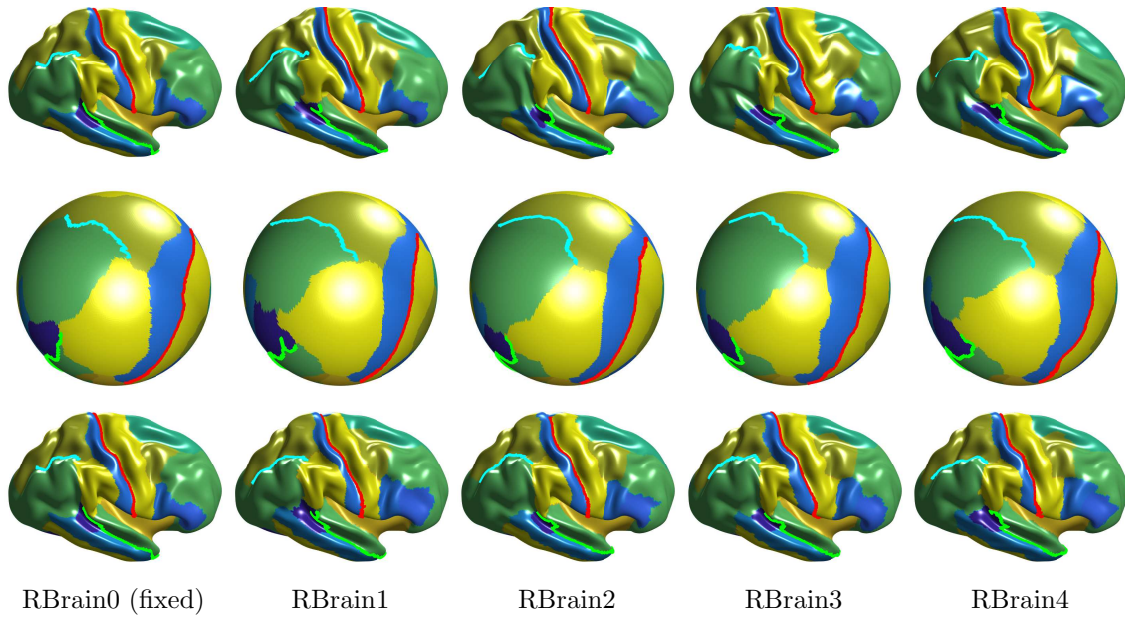


Figure 8: The right brains for registration, the registered spheres and the registered brains from top to bottom with $\lambda = 5$. The curves in red, green and cyan are the landmark curves.

Mesh	λ	Conformal energy	Angle distortion		Registration loss
			Mean	SD	
RBrain1	1	1.31e-03	3.56e-01	3.13e-01	4.95e-03
	5	3.41e-03	5.53e-01	5.27e-01	3.55e-03
	10	4.73e-03	6.28e-01	6.21e-01	1.39e-03
RBrain2	1	1.18e-03	3.50e-01	3.20e-01	4.35e-03
	5	3.00e-03	5.31e-01	5.43e-01	3.90e-03
	10	8.31e-03	7.55e-01	8.92e-01	3.00e-03
RBrain3	1	9.98e-04	3.28e-01	2.89e-01	3.87e-03
	5	2.34e-03	4.69e-01	4.42e-01	2.66e-03
	10	5.28e-03	5.86e-01	6.55e-01	1.83e-03
RBrain4	1	1.05e-03	3.35e-01	3.02e-01	2.67e-03
	5	2.63e-03	4.93e-01	4.82e-01	3.04e-03
	10	6.65e-03	7.38e-01	7.41e-01	2.40e-03

Table 5: The conformal energies, angle distortions and registration losses of registered brain surfaces with $\lambda = 1, 5, 10$, respectively.

7 Conclusions

In this paper, we employ spherical coordinates and directly solve the spherical CEM problem for the computation of the surface conformal parameterization. Then, we give the explicit derivations of the gradient vector and the Hessian matrix of the discrete conformal energy, which preserves the sparsity as the Laplacian matrix. Due to the sparsity of the Hessian matrix, the robust algorithm, called HBTR, is developed to solve the spherical CEM problem. HBTR sufficiently combines the local

quadratic convergence and continuing descent advantages of the gradient and the Newton directions. The numerical experiments actually show the conformality, the robustness and the local quadratic convergence of the HBTR. For the discrete scheme, we also present the quadratic convergence of the discrete conformal energy to the continuous scheme. Since the gradient vector and Hessian matrix of the registration loss have simple representations, we utilize the HBTR to propose a modified version of HBTR for the application to surface registrations. Significantly, the modified algorithm 3 also has quadratic convergence, suggesting its potential for extension to other applications of our method.

Acknowledgements

T. Li was supported in parts by the National Natural Science Foundation of China (NSFC) 12371377. W.-W. Lin was partially supported by the Ministry of Science and Technology (MoST 110-2115-M-A49-004), Taiwan. This work was partially supported by National Centre of Theoretical Sciences (NCTS) in Taiwan. We thank Tianhe-2 and the Big Data Computing Center in Southeast University, China, for their support of our use of their computing resources.

References

- [1] ALICE. <http://alice.loria.fr/>. (2016).
- [2] Digital Shape Workbench - Shape Repository. <http://visionair.ge.imati.cnr.it/ontologies/shapes/>. (2016).
- [3] Gary P. T. Choi’s website. <https://www.math.cuhk.edu.hk/~ptchoi/>. (2023).
- [4] Human Connectome Project. <http://www.humanconnectome.org>. (2023).
- [5] The Stanford 3D Scanning Repository. <http://graphics.stanford.edu/data/3Dscanrep/>. (2023).
- [6] TurboSquid. <https://www.turbosquid.com/>. (2023).
- [7] David Xianfeng Gu’s website. <http://www3.cs.stonybrook.edu/~gu/>, (2017).
- [8] Iso2Mesh. <http://iso2mesh.sourceforge.net>, (2018).
- [9] Emil Praun Alla Sheffer and Kenneth Rose. Mesh parameterization methods and their applications. *Foundations and Trends in Computer Graphics and Vision*, 2(2):105–171, 2006.
- [10] Pierre Alliez, Giuliana Ucelli, Craig Gotsman, and Marco Attene. Recent advances in remeshing of surfaces. In *Shape Analysis and Structuring*, pages 53–82. Springer Berlin Heidelberg, 2008.
- [11] Spyridon Bakas, Ujjwal Baid, Keyvan Farahani, et al. The International Brain Tumor Segmentation (BraTS) Cluster of Challenges, 2023.
- [12] Lévy Bruno, Petitjean Sylvain, Ray Nicolas, and Maillot Jérôme. Least squares conformal maps for automatic texture atlas generation. *ACM Transactions on Graphics*, 21(3):362–371, 2002.
- [13] Richard H. Byrd, Robert B. Schnabel, and Gerald A. Shultz. Approximate solution of the trust region problem by minimization over two-dimensional subspaces. *Mathematical Programming*, 40(1-3):247–263, 1988.
- [14] Gary P. T. Choi, Yusan Leung-Liu, Xianfeng Gu, and Lok Ming Lui. Parallelizable global conformal parameterization of simply-connected surfaces via partial welding. *SIAM Journal on Imaging Sciences*, 13(3):1049–1083, 2020.
- [15] Pui Tung Choi, Ka Chun Lam, and Lok Ming Lui. Flash: Fast landmark aligned spherical harmonic parameterization for genus-0 closed brain surfaces. *SIAM Journal on Imaging Sciences*, 8(1):67–94, 2015.
- [16] Mathieu Desbrun, Mark Meyer, and Pierre Alliez. Intrinsic parameterizations of surface meshes. *Computer Graphics Forum*, 21(3):209–218, 2002.

- [17] Darren Engwirda. *Locally optimal Delaunay-refinement and optimisation-based mesh generation*. PhD thesis, School of Mathematics and Statistics, The University of Sydney, 2014.
- [18] Darren Engwirda. Voronoi-based point-placement for three-dimensional delaunay-refinement. *Procedia Engineering*, 124:330–342, 2015.
- [19] Darren Engwirda. Conforming restricted delaunay mesh generation for piecewise smooth complexes. *Procedia Engineering*, 163:84–96, 2016.
- [20] Darren Engwirda. Generalised primal-dual grids for unstructured co-volume schemes. *Journal of Computational Physics*, 375:155–176, 2018.
- [21] Darren Engwirda and David Ivers. Off-centre steiner points for delaunay-refinement on curved surfaces. *Computer-Aided Design*, 72:157–171, 2016.
- [22] Hossein Eskandari. Strictly conformal transformation optics for directivity enhancement and unidirectional cloaking of a cylindrical wire antenna. *Scientific Reports*, 12(1), 2022.
- [23] Qianqian Fang and David A. Boas. Tetrahedral mesh generation from volumetric binary and grayscale images. In *2009 IEEE International Symposium on Biomedical Imaging: From Nano to Macro*. IEEE, 2009.
- [24] Michael S. Floater. Mean value coordinates. *Computer Aided Geometric Design*, 20(1):19–27, 2003.
- [25] Michael S. Floater and Kai Hormann. Surface parameterization: a tutorial and survey. In *Advances in Multiresolution for Geometric Modelling*, pages 157–186. Springer Berlin Heidelberg, 2005.
- [26] Mark Gillespie, Boris Springborn, and Keenan Crane. Discrete conformal equivalence of polyhedral surfaces. *ACM Transactions on Graphics*, 40(4):1–20, 2021.
- [27] Xianfeng Gu, Yalin Wang, Tony F. Chan, Paul M. Thompson, and Shing-Tung Yau. Genus zero surface conformal mapping and its application to brain surface mapping. *IEEE Transactions on Medical Imaging*, 23(8):949–958, 2004.
- [28] Xianfeng Gu and Shing-Tung Yau. *Computational Conformal Geometry*, volume 3 of *Advanced Lectures in Mathematics*. International Press and Higher Education Press, 2007.
- [29] Xianfeng Gu and Shing-Tung Yau. *Computational Conformal Geometry*. International Press and Higher Education Press, 2020.
- [30] Xianfeng David Gu, Wei Zeng, Feng Luo, and Shing-Tung Yau. Numerical computation of surface conformal mappings. *Computational Methods and Function Theory*, 11(2):747–787, 2011.
- [31] Krishna Chaitanya Gurijala, Rui Shi, Wei Zeng, Xianfeng Gu, and Arie Kaufman. Colon flattening using heat diffusion riemannian metric. *IEEE Transactions on Visualization and Computer Graphics*, 19(12):2848–2857, 2013.
- [32] Steven Haker, Sigurd Angenent, Allen Tannenbaum, Ron Kikinis, Guillermo Sapiro, and Michael Halle. Conformal surface parameterization for texture mapping. *IEEE Transactions on Visualization and Computer Graphics*, 6(2):181–189, 2000.
- [33] Kai Hormann, Bruno Lévy, and Alla Sheffer. Mesh parameterization: Theory and practice. In *ACM SIGGRAPH Course Notes*, 2007.
- [34] Wei-Qiang Huang, Xianfeng David Gu, Tsung-Ming Huang, Song-Sun Lin, Wen-Wei Lin, and Shing-Tung Yau. High performance computing for spherical conformal and riemann mappings. *Geometry, Imaging and Computing*, 1(2):223–258, 2014.
- [35] John E. Hutchinson. Computing conformal maps and minimal surfaces. *Proceedings of the Centre for Mathematics and its Applications*, 26:140–161, 1991.
- [36] Miao Jin, Junho Kim, Feng Luo, and Xianfeng Gu. Discrete surface ricci flow. *IEEE Transactions on Visualization and Computer Graphics*, 14(5):1030–1043, 2008.

- [37] Yueh-Cheng Kuo, Wen-Wei Lin, Mei-Heng Yueh, and Shing-Tung Yau. Convergent conformal energy minimization for the computation of disk parameterizations. *SIAM Journal on Imaging Sciences*, 14(4):1790–1815, 2021.
- [38] Rongjie Lai, Zaiwen Wen, Wotao Yin, Xianfeng Gu, and Lok Ming Lui. Folding-free global conformal mapping for genus-0 surfaces by harmonic energy minimization. *Journal of Scientific Computing*, 58(3):705–725, 2014.
- [39] Jingxin Nie, Tianming Liu, Gang Li, Geoffrey Young, Ashley Tarokh, Lei Guo, and Stephen T.C. Wong. Least-square conformal brain mapping with spring energy. *Computerized Medical Imaging and Graphics*, 31(8):656–664, 2007.
- [40] Ulrich Pinkall and Konrad Polthier. Computing discrete minimal surfaces and their conjugates. *Experimental Mathematics*, 2(15):15–36, 1993.
- [41] Rohan Sawhney and Keenan Crane. Boundary first flattening. *ACM Transactions on Graphics*, 37(1):5:1–5:14, 2017.
- [42] Rui Shi, Wei Zeng, Zhengyu Su, Jian Jiang, Hanna Damasio, Zhonglin Lu, Yalin Wang, Shing-Tung Yau, and Xianfeng Gu. Hyperbolic harmonic mapping for surface registration. *IEEE Transactions on Pattern Analysis and Machine Intelligence*, 39(5):965–980, 2017.
- [43] Gerald A. Shultz, Robert B. Schnabel, and Richard H. Byrd. A family of trust-region-based algorithms for unconstrained minimization with strong global convergence properties. *SIAM Journal on Numerical Analysis*, 22(1):47–67, 1985.
- [44] Anh Phong Tran, Shijie Yan, and Qianqian Fang. Improving model-based functional near-infrared spectroscopy analysis using mesh-based anatomical and light-transport models. *Neurophotonics*, 7(01):1, 2020.
- [45] Lin Xu and Huanyang Chen. Conformal transformation optics. *Nature Photonics*, 9(1):15–23, 2014.
- [46] Yong-Liang Yang, Ren Guo, Feng Luo, Shi-Min Hu, and Xianfeng Gu. Generalized discrete ricci flow. *Computer Graphics Forum*, 28(7):2005–2014, 2009.
- [47] Mei-Heng Yueh, Tsung-Ming Huang, Tiexiang Li, Wen-Wei Lin, and Shing-Tung Yau. Projected gradient method combined with homotopy techniques for volume-measure-preserving optimal mass transportation problems. *Journal of Scientific Computing*, 88(3), 2021.
- [48] Mei-Heng Yueh, Tiexiang Li, Wen-Wei Lin, and Shing-Tung Yau. A novel algorithm for volume-preserving parameterizations of 3-manifolds. *SIAM Journal on Imaging Sciences*, 12(2):1071–1098, 2019.
- [49] Mei-Heng Yueh, Wen-Wei Lin, Chin-Tien Wu, and Shing-Tung Yau. An efficient energy minimization for conformal parameterizations. *Journal of Scientific Computing*, 73(1):203–227, 2017.